MIT Open Access Articles

The SPTPoL extended cluster survey

As Published	10.3847/1538-4365/ab6993
Publisher	American Astronomical Society
Version	Final published version
Citable link	https://hdl.handle.net/1721.1/132341
Terms of Use	Article is made available in accordance with the publisher's policy and may be subject to US copyright law. Please refer to the publisher's site for terms of use.

CrossMark

The SPTpol Extended Cluster Survey

L. E. Bleem[1,2], S. Bocquet[1,2,3], B. Stalder[4,5], M. D. Gladders[2,6], P. A. R. Ade[7], S. W. Allen[8,9,10], A. J. Anderson[11],
J. Annis[11], M. L. N. Ashby[5], J. E. Austermann[12], S. Avila[13], J. S. Avva[14], M. Bayliss[15,16], J. A. Beall[12], K. Bechtol[4,17],
A. N. Bender[1,2], B. A. Benson[2,6,11], E. Bertin[18,19], F. Bianchini[20], C. Blake[21], M. Brodwin[22], D. Brooks[23],
E. Buckley-Geer[11], D. L. Burke[8,10], J. E. Carlstrom[1,2,6,24,25], A. Carnero Rosell[26,27], M. Carrasco Kind[28,29],
J. Carretero[30], C. L. Chang[1,2,6], H. C. Chiang[31,32], R. Citron[33], C. Corbett Moran[33,34], M. Costanzi[35,36], T. M. Crawford[2,6],
A. T. Crites[2,6,37], L. N. da Costa[27,38], T. de Haan[14,39], J. De Vicente[26], S. Desai[40], H. T. Diehl[11], J. P. Dietrich[3,41],
M. A. Dobbs[31,42], T. F. Eifler[43,44], W. Everett[45], B. Flaugher[11], B. Floyd[22], J. Frieman[2,11], J. Gallicchio[2,46],
J. García-Bellido[13], E. M. George[14,47], D. W. Gerdes[48,49], A. Gilbert[31], D. Gruen[8,9,10], R. A. Gruendl[28,29],
J. Gschwend[27,38], N. Gupta[20], G. Gutierrez[11], N. W. Halverson[45,50], N. Harrington[14], J. W. Henning[1,2], C. Heymans[51,52],
G. P. Holder[42,53,54], D. L. Hollowood[55], W. L. Holzapfel[14], K. Honscheid[56,57], J. D. Hrubes[33], N. Huang[14], J. Hubmayr[12],
K. D. Irwin[9,10], D. J. James[5], T. Jeltema[55], S. Joudaki[58], G. Khullar[2,6], M. Klein[3,59], L. Knox[60], N. Kuropatkin[11],
A. T. Lee[14,39], D. Li[10,12], C. Lidman[61], A. Lowitz[6], N. MacCrann[56,57], G. Mahler[48], M. A. G. Maia[27,38], J. L. Marshall[62],
M. McDonald[15], J. J. McMahon[49], P. Melchior[63], F. Menanteau[28,29], S. S. Meyer[2,6,24,25], R. Miquel[30,64],
L. M. Mocanu[2,6,65], J. J. Mohr[3,41,59], J. Montgomery[31], A. Nadolski[53,54], T. Natoli[2,6], J. P. Nibarger[12], G. Noble[31], V. Novosad[66],
S. Padin[2,6,37], A. Palmese[11], D. Parkinson[67], S. Patil[20], F. Paz-Chinchón[28,29], A. A. Plazas[63], C. Pryke[68],
N. S. Ramachandra[1,2], C. L. Reichardt[20], J. D. Remolina González[48], A. K. Romer[69], A. Roodman[8,10], J. E. Ruhl[70],
E. S. Rykoff[8,10], B. R. Saliwanchik[71], E. Sanchez[26], A. Saro[35,36,72], J. T. Sayre[45,50], K. K. Schaffer[2,25,73], T. Schrabback[74],
S. Serrano[75,76], K. Sharon[48], C. Sievers[33], G. Smecher[31,77], M. Smith[78], M. Soares-Santos[79], A. A. Stark[5], K. T. Story[8,9],
E. Suchyta[80], G. Tarle[49], C. Tucker[7], K. Vanderlinde[81,82], T. Veach[83], J. D. Vieira[53,54], G. Wang[1], J. Weller[3,41,59],
N. Whitehorn[84], W. L. K. Wu[2], V. Yefremenko[1], and Y. Zhang[11]

[1] High Energy Physics Division, Argonne National Laboratory, 9700 South Cass Avenue, Lemont, IL 60439, USA; lbleem@anl.gov
[2] Kavli Institute for Cosmological Physics, University of Chicago, 5640 South Ellis Avenue, Chicago, IL 60637, USA
[3] Department of Physics, Ludwig-Maximilians-Universität, Scheinerstr. 1, D-81679 München, Germany
[4] LSST, 933 North Cherry Avenue, Tucson, AZ 85721, USA
[5] Center for Astrophysics|Harvard & Smithsonian, 60 Garden Street, Cambridge, MA 02138, USA
[6] Department of Astronomy and Astrophysics, University of Chicago, 5640 South Ellis Avenue, Chicago, IL 60637, USA
[7] Cardiff University, Cardiff CF10 3XQ, UK
[8] Kavli Institute for Particle Astrophysics & Cosmology, P.O. Box 2450, Stanford University, Stanford, CA 94305, USA
[9] Department of Physics, Stanford University, 382 Via Pueblo Mall, Stanford, CA 94305, USA
[10] SLAC National Accelerator Laboratory, 2575 Sand Hill Road, Menlo Park, CA 94025, USA
[11] Fermi National Accelerator Laboratory, P.O. Box 500, Batavia, IL 60510, USA
[12] NIST Quantum Devices Group, 325 Broadway Mailcode 817.03, Boulder, CO 80305, USA
[13] Instituto de Fisica Teorica UAM/CSIC, Universidad Autonoma de Madrid, E-28049 Madrid, Spain
[14] Department of Physics, University of California, Berkeley, CA 94720, USA
[15] Kavli Institute for Astrophysics and Space Research, Massachusetts Institute of Technology, 77 Massachusetts Avenue, Cambridge, MA 02139, USA
[16] Department of Physics, University of Cincinnati, Cincinnati, OH 45221, USA
[17] Physics Department, 2320 Chamberlin Hall, University of Wisconsin-Madison, 1150 University Avenue Madison, WI 53706-1390, USA
[18] CNRS, UMR 7095, Institut d'Astrophysique de Paris, F-75014, Paris, France
[19] Sorbonne Universités, UPMC Univ Paris 06, UMR 7095, Institut d'Astrophysique de Paris, F-75014, Paris, France
[20] School of Physics, University of Melbourne, Parkville, VIC 3010, Australia
[21] Centre for Astrophysics & Supercomputing, Swinburne University of Technology, P.O. Box 218, Hawthorn, VIC 3122, Australia
[22] Department of Physics and Astronomy, University of Missouri, 5110 Rockhill Road, Kansas City, MO 64110, USA
[23] Department of Physics & Astronomy, University College London, Gower Street, London, WC1E 6BT, UK
[24] Department of Physics, University of Chicago, 5640 South Ellis Avenue, Chicago, IL 60637, USA
[25] Enrico Fermi Institute, University of Chicago, 5640 South Ellis Avenue, Chicago, IL 60637, USA
[26] Centro de Investigaciones Energéticas, Medioambientales y Tecnológicas (CIEMAT), Madrid, Spain
[27] Laboratório Interinstitucional de e-Astronomia—LIneA, Rua Gal. José Cristino 77, Rio de Janeiro, RJ—20921-400, Brazil
[28] Department of Astronomy, University of Illinois at Urbana-Champaign, 1002 W. Green Street, Urbana, IL 61801, USA
[29] National Center for Supercomputing Applications, 1205 West Clark St., Urbana, IL 61801, USA
[30] Institut de Física d'Altes Energies (IFAE), The Barcelona Institute of Science and Technology, Campus UAB, E-08193 Bellaterra (Barcelona) Spain
[31] Department of Physics, McGill University, 3600 Rue University, Montreal, QC H3A 2T8, Canada
[32] School of Mathematics, Statistics & Computer Science, University of KwaZulu-Natal, Durban, South Africa
[33] University of Chicago, 5640 South Ellis Avenue, Chicago, IL 60637, USA
[34] TAPIR, Walter Burke Institute for Theoretical Physics, California Institute of Technology, 1200 E. California Blvd., Pasadena 91125, CA, USA
[35] INAF-Osservatorio Astronomico di Trieste, via G.B. Tiepolo 11, I-34143 Trieste, Italy
[36] Institute for Fundamental Physics of the Universe, Via Beirut 2, I-34014 Trieste, Italy
[37] California Institute of Technology, MS 249-17, 1216 E. California Blvd., Pasadena, CA 91125, USA
[38] Observatório Nacional, Rua Gal. José Cristino 77, Rio de Janeiro, RJ—20921-400, Brazil
[39] Physics Division, Lawrence Berkeley National Laboratory, Berkeley, CA 94720, USA
[40] Department of Physics, IIT Hyderabad, Kandi, Telangana 502285, India
[41] Excellence Cluster Universe, Boltzmannstr. 2, D-85748 Garching, Germany
[42] Canadian Institute for Advanced Research, CIFAR Program in Gravity and the Extreme Universe, Toronto, ON M5G 1Z8, Canada
[43] Department of Astronomy/Steward Observatory, University of Arizona, 933 North Cherry Avenue, Tucson, AZ 85721-0065, USA
[44] Jet Propulsion Laboratory, California Institute of Technology, 4800 Oak Grove Dr., Pasadena, CA 91109, USA
[45] Department of Astrophysical and Planetary Sciences, University of Colorado, Boulder, CO 80309, USA

[46] Harvey Mudd College, 301 Platt Blvd., Claremont 91711, CA, USA

[47] European Southern Observatory, Karl-Schwarzschild-Str. 2, D-85748 Garching bei München, Germany

[48] Department of Astronomy, University of Michigan, 1085 S. University Ave., Ann Arbor, MI 48109, USA

[49] Department of Physics, University of Michigan, 450 Church Street, Ann Arbor, MI 48109, USA

[50] Department of Physics, University of Colorado, Boulder, CO 80309, USA

[51] Institute for Astronomy, University of Edinburgh, Royal Observatory, Blackford Hill, Edinburgh EH9 3HJ, UK

[52] German Centre for Cosmological Lensing (GCCL), Astronomisches Institut, Ruhr-Universität Bochum, Universitätsstr. 150, D-44801 Bochum, Germany

[53] Department of Physics, University of Illinois Urbana-Champaign, 1110 W. Green Street, Urbana, IL 61801, USA

[54] Astronomy Department, University of Illinois at Urbana-Champaign, 1002 W. Green Street, Urbana, IL 61801, USA

[55] Santa Cruz Institute for Particle Physics, Santa Cruz, CA 95064, USA

[56] Center for Cosmology and Astro-Particle Physics, The Ohio State University, Columbus, OH 43210, USA

[57] Department of Physics, The Ohio State University, Columbus, OH 43210, USA

[58] Department of Physics, University of Oxford, Denys Wilkinson Building, Keble Road, Oxford OX1 3RH, UK

[59] Max-Planck-Institut für extraterrestrische Physik, Giessenbachstr. D-85748 Garching, Germany

[60] Department of Physics, University of California, One Shields Avenue, Davis, CA 95616, USA

[61] The Research School of Astronomy and Astrophysics, Australian National University, ACT 2601, Australia

[62] George P. and Cynthia Woods Mitchell Institute for Fundamental Physics and Astronomy, and Department of Physics and Astronomy, Texas A&M University, College Station, TX 77843, USA

[63] Department of Astrophysical Sciences, Princeton University, Peyton Hall, Princeton, NJ 08544, USA

[64] Institució Catalana de Recerca i Estudis Avançats, E-08010 Barcelona, Spain

[65] Institute of Theoretical Astrophysics, University of Oslo, P.O. Box 1029 Blindern, NO-0315 Oslo, Norway

[66] Materials Sciences Division, Argonne National Laboratory, 9700 South Cass Avenue, Lemont, IL 60439, USA

[67] Korea Astronomy and Space Science Institute, 776 Daedeokdae-ro, Yuseong-gu, Daejeon 34055, Republic of Korea

[68] School of Physics and Astronomy, University of Minnesota, 116 Church Street S.E., Minneapolis, MN 55455, USA

[69] Department of Physics and Astronomy, Pevensey Building, University of Sussex, Brighton, BN1 9QH, UK

[70] Physics Department, Center for Education and Research in Cosmology and Astrophysics, Case Western Reserve University, Cleveland, OH 44106, USA

[71] Department of Physics, Yale University, 217 Prospect Street, New Haven, CT 06511, USA

[72] Astronomy Unit, Department of Physics, University of Trieste, via Tiepolo 11, I-34131 Trieste, Italy

[73] Liberal Arts Department, School of the Art Institute of Chicago, 112 S. Michigan Ave., Chicago, IL 60603, USA

[74] Argelander-Institut für Astronomie, Universität Bonn, Auf dem Hügel 71, D-53121, Bonn, Germany

[75] Institut d'Estudis Espacials de Catalunya (IEEC), E-08034 Barcelona, Spain

[76] Institute of Space Sciences (ICE, CSIC), Campus UAB, Carrer de Can Magrans, s/n, E-08193 Barcelona, Spain

[77] Three-Speed Logic, Inc., Victoria, B.C., V8S 3Z5, Canada

[78] School of Physics and Astronomy, University of Southampton, Southampton, SO17 1BJ, UK

[79] Brandeis University, Physics Department, 415 South Street, Waltham MA 02453, USA

[80] Computer Science and Mathematics Division, Oak Ridge National Laboratory, Oak Ridge, TN 37831, USA

[81] Dunlap Institute for Astronomy & Astrophysics, University of Toronto, 50 St George St., Toronto, ON M5S 3H4, Canada

[82] Department of Astronomy & Astrophysics, University of Toronto, 50 St George St, Toronto, ON M5S 3H4, Canada

[83] Department of Astronomy, University of Maryland, College Park, MD 20742, USA

[84] Department of Physics and Astronomy, University of California, Los Angeles, CA 90095, USA

Abstract

We describe the observations and resultant galaxy cluster catalog from the 2770 deg^2 SPTpol Extended Cluster Survey (SPT-ECS). Clusters are identified via the Sunyaev–Zel'dovich (SZ) effect and confirmed with a combination of archival and targeted follow-up data, making particular use of data from the Dark Energy Survey (DES). With incomplete follow-up we have confirmed as clusters 244 of 266 candidates at a detection significance $\xi \geqslant 5$ and an additional 204 systems at $4 < \xi < 5$. The confirmed sample has a median mass of $M_{500c} \sim 4.4 \times 10^{14} M_\odot h_{70}^{-1}$ and a median redshift of $z = 0.49$, and we have identified 44 strong gravitational lenses in the sample thus far. Radio data are used to characterize contamination to the SZ signal; the median contamination for confirmed clusters is predicted to be $\sim 1\%$ of the SZ signal at the $\xi > 4$ threshold, and $<4\%$ of clusters have a predicted contamination $>10\%$ of their measured SZ flux. We associate SZ-selected clusters, from both SPT-ECS and the SPT-SZ survey, with clusters from the DES redMaPPer sample, and we find an offset distribution between the SZ center and central galaxy in general agreement with previous work, though with a larger fraction of clusters with significant offsets. Adopting a fixed *Planck*-like cosmology, we measure the optical richness–SZ mass ($\lambda - M$) relation and find it to be 28% shallower than that from a weak-lensing analysis of the DES data—a difference significant at the 4σ level—with the relations intersecting at $\lambda = 60$. The SPT-ECS cluster sample will be particularly useful for studying the evolution of massive clusters and, in combination with DES lensing observations and the SPT-SZ cluster sample, will be an important component of future cosmological analyses.

Unified Astronomy Thesaurus concepts: Galaxy clusters (584); Strong gravitational lensing (1643); Large-scale structure of the universe (902)

Supporting material: machine-readable tables

1. Introduction

Clusters of galaxies, as tracers of the extreme peaks in the matter density field, are valuable tools for constraining cosmological and astrophysical models (see, e.g., Voit 2005; Allen et al. 2011; Kravtsov & Borgani 2012; Weinberg et al. 2013, and references therein). Clusters imprint signals on the sky across the electromagnetic spectrum, which have led to three main ways of observationally detecting these systems: as

overdensities of galaxies in optical and/or near-infrared (NIR) surveys (e.g., Abell 1958; Koester et al. 2007; Eisenhardt et al. 2008; Wen et al. 2012; Rykoff et al. 2014; Bleem et al. 2015a; Oguri et al. 2018; Wen et al. 2018; Gonzalez et al. 2019), as sources of extended extragalactic emission at X-ray wavelengths (e.g., Gioia et al. 1990; Böhringer et al. 2004; Ebeling et al. 2010; Piffaretti et al. 2011; Mehrtens et al. 2012; Liu et al. 2015b; Adami et al. 2018; Klein et al. 2019), and via their Sunyaev–Zel'dovich (SZ) signature (Sunyaev & Zel'dovich 1972) in millimeter-wave surveys. The last two techniques rely on observables arising from the hot (10^7–10^8 K) gas in the intracluster medium. While wide-field SZ cluster selection is the newest realized technique—with the first cluster blindly detected in millimeter-wave survey data in 2008 (Staniszewski et al. 2009)—the field has rapidly advanced, with over 1000 SZ-selected clusters published to date (Bleem et al. 2015b; Planck Collaboration et al. 2016b; Hilton et al. 2018; Huang et al. 2019). SZ-selected cluster samples from high-resolution millimeter-wave surveys are of particular interest, as they have low-scatter mass-observable proxies and, given the redshift independence of the thermal SZ surface brightness, are in principle mass limited (Carlstrom et al. 2002; Motl et al. 2005). Indeed, such samples have enabled SZ cluster cosmological results that are competitive (Hasselfield et al. 2013; Planck Collaboration et al. 2016c; Bocquet et al. 2019) with samples selected at other wavelengths (e.g., Vikhlinin et al. 2009; Mantz et al. 2010, 2015).

Cosmological constraints from samples of clusters are currently limited by an imperfect knowledge of both cluster selection and the connection of cluster observables to theoretical models. The multiwavelength nature of cluster signals allows for considerable opportunities to test and improve our understanding of these relations. Such explorations with SZ data and observations at other wavelengths can take many forms, including (a) the use of optical, NIR, and X-ray data to both confirm SZ cluster candidates and provide empirical tests of models of SZ selection (e.g., Andersson et al. 2011; Planck Collaboration et al. 2012, 2013; Bleem et al. 2015b; Liu et al. 2015a; Planck Collaboration et al. 2016b; Barrena et al. 2018; Burenin et al. 2018; Hilton et al. 2018); (b) using SZ data to probe X-ray samples (e.g., Czakon et al. 2015; Bender et al. 2016; Mantz et al. 2016); and (c) using SZ data to test mass–optical observable scaling relations (Planck Collaboration et al. 2011; Biesiadzinski et al. 2012; Sehgal et al. 2013; Rozo et al. 2014, 2015; Mantz et al. 2016; Saro et al. 2017; Jimeno et al. 2018). Multiwavelength observables are also used to constrain relevant quantities such as the spatial distribution of proxies for the cluster centers that feed into the derivation of such relations (e.g., Lin & Mohr 2004; George et al. 2012; Saro et al. 2015; Zhang et al. 2019).

In this work we expand the sample of SZ-selected clusters available for such studies using a new survey conducted using the SPTpol receiver (Austermann et al. 2012) on the South Pole Telescope (SPT). This wide and shallow survey complements the deeper surveys conducted with the SPT (Benson et al. 2014; Henning et al. 2018) and will provide additional overlap for the comparison of cluster properties with the ACTPol (De Bernardis et al. 2016) and *Planck* surveys. Here we present 266 cluster candidates detected at a signal-to-noise ratio (S/N) $\xi > 5$, 244 of which are confirmed as clusters using optical and NIR data, as well as via a search of the literature. We also report an additional 204 confirmed systems at $4 < \xi < 5$. Combining this data set with the previously published SPT-SZ cluster sample (Bleem et al. 2015b, hereafter B15), we use this expanded cluster sample to explore the SZ properties of massive optically selected clusters identified using the red-sequence Matched-filter Probabilistic Percolation (redMaPPer) algorithm (Rykoff et al. 2014) in the Dark Energy Survey (DES) Year 3 data set.

We organize this work as follows. In Section 2 we describe the survey observations and data reduction process. In Section 3 we describe the identification of cluster candidates, including checks on the radio contamination of the sample, and in Section 4 we describe the cluster confirmation process, including details on the external data sets used for this process. In Section 5 we present the full sample and several internal consistency checks with the SPT-SZ cluster sample. Detailed comparisons to the DES redMaPPer sample, including determination of the SZ−optical center offsets and SZ mass −optical richness relation, are presented in Section 6. We conclude in Section 7.

All optical magnitudes are quoted in the AB system (Oke 1974). Except when noted, all masses are reported in terms of M_{500c}, defined as the mass enclosed within a radius at which the average density is 500 times the critical density at the cluster redshift. We assume a fiducial spatially flat ΛCDM cosmology with $\sigma_8 = 0.80$, $\Omega_b = 0.046$, $\Omega_m = 0.30$, $h = 0.70$, $n_s(0.002) = 0.972$, and $\Sigma m_\nu = 0.06$ eV. The normal distribution with mean $\boldsymbol{\mu}$ and variance $\boldsymbol{\Sigma}$ is written as $\mathcal{N}(\boldsymbol{\mu}, \boldsymbol{\Sigma})$. Selected data reported in this work, as well as future updates to the properties of these clusters, will be hosted at http://pole.uchicago.edu/public/data/sptsz-clusters.

2. Millimeter-wave Observations and Data Processing

The SPTpol Extended Cluster Survey (SPT-ECS) is a 2770 deg^2 survey that covers two separate regions of sky with low dust emission that lie north of previous areas surveyed using the SPT: a 2200 deg^2 region bounded in right ascension (R.A.) and decl. (δ) by $22^h \leqslant$ R.A. $\leqslant 6^h$ and $-40° < \delta < -20°$, and a second 570 deg^2 region bounded by $10^h \leqslant$ R.A. $\leqslant 14^h$ and $-30° \leqslant \delta \leqslant -20°$. These observations—conducted during the 2013, 2014, and 2015 austral summer months when data from the main 500 deg^2 SPTpol survey field (centered at R.A $= 0^h$, $\delta = -57°.5$; see Henning et al. 2018) would have been contaminated by scattered sunlight—serve to significantly increase the overlap of data from the SPT with that from other surveys, including the DES (Flaugher et al. 2015), Kilo-Degree Survey (KIDS; de Jong et al. 2013), 2-degree Field Lensing Survey (2dFLenS; Blake et al. 2016), VISTA Kilo-Degree Infrared Galaxy Survey (VIKING, Edge et al. 2013), and *Herschel*-ATLAS (Eales et al. 2010); see Figure 1.

2.1. Observations

The survey was conducted using the SPTpol receiver that was installed on the 10 m SPT (Carlstrom et al. 2011) from 2012 to 2016. As detailed in Austermann et al. (2012), the receiver is composed of 768 feedhorn-coupled polarization-sensitive pixels split between the two channels with 588 pixels at 150 GHz and 180 pixels at 95 GHz; each pixel contains two transition-edge-sensor bolometers, resulting in 1536 detectors in total. The primary mirror is slightly underilluminated, resulting in beams well approximated by Gaussians with FWHM of 1′.2 and 1′.7 at 150 and 95 GHz, respectively.
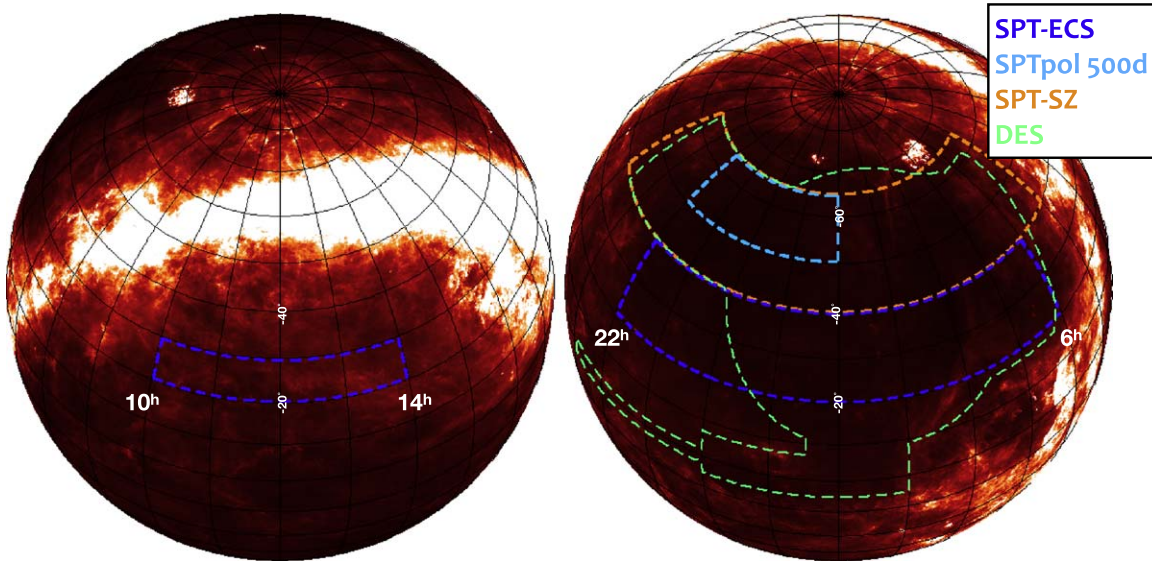
Figure 1. Footprint of the SPTpol Extended Cluster Survey (dark blue) as compared to the SPT-SZ (orange) and SPTpol 500d survey (light blue). Optical−NIR imaging from the Dark Energy Survey (green dashed region) covers ∼58% of the survey footprint and is used to confirm a significant number of survey clusters presented in this work. The survey outlines are overlaid on the *IRAS* 100 μm dust map (Schlegel et al. 1998), with the orthographic projection chosen such that the South Celestial Pole is at the top of the globe. Beyond DES, SPT-ECS also has significant overlap with the southern field of the Kilo-Degree Survey, the *Herschel*-ATLAS survey, and the 2dFLenS spectroscopic survey.

The survey is composed of 10 separate ∼250–270 deg^2 "fields," each imaged to noise levels of ∼30–40 μK arcmin at 150 GHz; see Table 1. The fields were observed by scanning the telescope at fixed elevation back and forth in azimuth at ∼0°.55 s^{-1}, stepping 10′ in elevation, and then scanning in azimuth again. This process is repeated until the full field is covered in a complete "observation." Each field was observed >80 times, and 20 different dithered elevation starting points were used to provide uniform coverage in the final co-added maps.

2.2. Data Processing

The data processing and mapmaking procedures in this work follow closely those in previous SPT-SZ and SPTpol publications (see, e.g., Schaffer et al. 2011; Bleem et al. 2015b; Crites et al. 2015; Henning et al. 2018). First, for each observation, the time-ordered bolometer data (TOD) is corrected for electrical cross talk between detectors, and a small amount of bandwidth (∼1.4 Hz and harmonics) is notch-filtered to remove spurious signals from the pulse tube coolers that cool the optics and receiver cryostats. Next, using the cut criteria detailed in Crites et al. (2015), detectors with poor noise performance, poor responsivity to optical sources, and/or anomalous jumps in TOD are removed. As this work is focused on temperature-based science, we relax the requirement that both bolometers in a pixel polarization pair be active for an observation. Relative gains across the array are then normalized using a combination of regular observations of both an internal calibrator source and the galactic H II region RCW 38. For the first field observed in the survey—RA23HDEC−35[85]—the internal calibrator was inadvertently disabled during summer maintenance for ∼50% of the observations, and so these data were relatively calibrated only with RCW 38 observations.

The TOD is then processed on a per-azimuth scan basis by fitting and subtracting a seventh-order Legendre polynomial,

Table 1
Summary Information for the 10 Fields That Compose the 2770 deg^2 SPTpol Extended Cluster Survey

Name	R.A. (deg)	δ (deg)	Area (deg^2)	σ_{95} (μK arcmin)	σ_{150} (μK arcmin)	γ_{field}
RA23HDEC-25	345.0	−25.0	276.0	61.3	30.5	0.84
RA23HDEC-35	345.0	−35.0	250.2	59.4	36.6	0.80
RA1HDEC-25	15.0	−25.0	275.2	80.4	39.2	0.69
RA1HDEC-35	15.0	−35.0	251.8	61.5	36.6	0.79
RA3HDEC-25	45.0	−25.0	272.9	54.6	28.6	0.90
RA3HDEC-35	45.0	−35.0	248.8	43.8	25.3	1.04
RA5HDEC-25	75.0	−25.0	277.0	57.0	31.4	0.85
RA5HDEC-35	75.0	−35.0	250.3	54.8	31.6	0.88
RA11HDEC-25	165.0	−25.0	274.3	77.6	40.0	0.68
RA13HDEC-25	195.0	−25.0	270.8	50.7	30.0	0.90

Note. Listed are the field name, center, source-masked effective area, and noise levels at both 95 and 150 GHz, as well as the "field renormalization" factors discussed in Section 5.1.1. The survey contains an additional 122 deg^2 that are masked in the cluster analysis owing to the presence of millimeter-bright sources. Following Schaffer et al. (2011), the noise levels are measured from $4000 < \ell < 5000$ using a Gaussian beam approximation with FWHM of 1.7 (1.2) arcmin at 95 (150) GHz. The field renormalization factors are normalized with respect to the values from Reichardt et al. (2013) and de Haan et al. (2016) for the SPT-SZ survey.

applying an isotropic common mode filter that removes the mean of all detectors in a given frequency, high-passing the data at angular multipole $\ell = 300$ and low-passing the data at $\ell = 20,000$. Sources detected in preliminary mapmaking runs at $\geqslant 5\sigma$ (∼9–15 mJy depending on field depth) at 150 GHz and bright radio sources detected in the Australia Telescope 20-GHz Survey (AT20G; Murphy et al. 2010) at the edges of the field are masked with a 4′ radius during these filtering steps. The SPT-ECS also contains a small number of sources with extended millimeter-wave emission (see Section 3.2) and more conservative masks around these sources are applied in

---

[85] SPT fields are named for their central coordinates.

the filtering steps.[86] Following filtering, the TOD for each detector is then weighted based on the inverse noise variance in the 1–3 Hz signal band and binned into $0\farcs25$ pixels in maps in the Sanson-Flamsteed projection (Calabretta & Greisen 2002) using reconstructed telescope pointing. We have extended the characterization of the SPT pointing model to incorporate position information from all millimeter-wave-bright AT20G sources (typically 45–60 sources per field detected at S/N > 10 were used, compared to the two to three bright sources that proved sufficient in previous SPT analyses) to better constrain boom flexure and other mechanical aspects of the telescope at the elevations of these fields. With this extension we achieve reconstructed pointing performance of $\sim3''$–$4''$ rms when comparing SPT source locations to AT20G positions.

The single-observation maps for each field are then characterized based on both noise properties and coverage; maps with significant outliers from the median of these distributions are flagged and excluded from the co-addition step. The remaining maps are combined in a weighted sum based on their total pixel weights from the previous binning step; final maps consist of 78–150 observations per field.

The SPT-ECS fields were taken at significantly higher levels of atmospheric loading compared to other SPTpol survey data.[87] We found it necessary to augment our standard absolute calibration process (see, e.g., Staniszewski et al. 2009) with two additional steps that make use of the 143 GHz full- and half-mission temperature maps from the 2015 *Planck* data release (Planck Collaboration et al. 2015, 2016a). The first step follows a similar method to the absolute temperature calibration conducted in previous SPT power spectrum analyses (e.g., Henning et al. 2018; Hou et al. 2018). We derive normalization factors to rescale each co-added map by first convolving the *Planck* maps with the SPT beams and transfer functions (the latter resulting from the TOD filtering process described above) and the SPT maps with the *Planck* beam and window function. Then, masking bright point sources in the field, we set the normalization as the ratio from $900 \leqslant \ell \leqslant 1600$ of the cross spectrum of the *Planck* half-mission maps to the cross spectrum of the *Planck* full-mission map with the SPT maps. The 95 GHz data required an additional calibration step, as we found—especially in the fields centered at $\delta = -25°$—that the responsivity of the detectors decreased with increasing air mass. This trend is well represented as a linear decline in sensitivity as a function of decl., and we used the *Planck* data to fit for and correct this variation across the fields.

3. Cluster Identification

Identification of cluster candidates in the SPT-ECS proceeds in essentially identical fashion to previous SPT analyses (see, e.g., B15 for a recent example). This section provides an overview of the process; readers are referred to previous publications for more details.

3.1. Sky Model and Matched Filter

The thermal SZ signal is produced by the inverse Compton scattering of cosmic microwave background (CMB) photons off high-energy electrons, such as those that reside in the intracluster medium of galaxy clusters. This produces a spectral distortion of the observed CMB temperature at the location x of clusters given by the line-of-sight integral (Sunyaev & Zel'dovich 1972)

$$\Delta T(\boldsymbol{x}, \nu) = T_{\mathrm{CMB}} f_{\mathrm{SZ}}(\nu) \int n_{\mathrm{e}}(\boldsymbol{r}) \frac{k_{\mathrm{B}} T_{\mathrm{e}}(\boldsymbol{r})}{m_{\mathrm{e}} c^2} \sigma_{\mathrm{T}} dl$$
$$\equiv T_{\mathrm{CMB}} f_{\mathrm{SZ}}(\nu)\, y_{\mathrm{SZ}}(\boldsymbol{x}), \qquad (1)$$

where $T_{\mathrm{CMB}} = 2.7260 \pm 0.0013$ K is the mean CMB temperature (Fixsen 2009), $f_{\mathrm{SZ}}(\nu)$ is the frequency (ν) dependence of the thermal SZ effect (Sunyaev & Zel'dovich 1980), n_{e} is the electron density, T_{e} is the electron temperature, k_{B} is the Boltzmann constant, $m_{\mathrm{e}} c^2$ is the electron rest-mass energy, σ_{T} is the Thomson cross section, and y_{SZ} is the Compton y-parameter. This effect results in a decrement at the two channels measured by the SPTpol receiver; for a nonrelativistic thermal SZ spectrum the effective band centers are 95.9 and 148.5 GHz.[88]

To identify candidate galaxy clusters, we use a spatial-spectral filter designed to optimally extract thermal SZ cluster signals (Melin et al. 2006). This "matched-filter" approach has been widely used both in previous SPT publications and in analyses by other experiments (see, e.g., Planck Collaboration et al. 2016b; Hilton et al. 2018). We model the cluster profile as a projected spherical β-model with β fixed to 1 (Cavaliere & Fusco-Femiano 1976):

$$\Delta T = \Delta T_0 (1 + \theta^2/\theta_{\mathrm{c}}^2)^{-(3\beta-1)/2}, \qquad (2)$$

where the normalization ΔT_0 is a free parameter and the core radius, θ_{c}, is allowed to vary in 12 equally spaced steps from $0\farcs25$ to $3'$.

3.2. Masking

To prevent spurious decrements from the filtering process, we mask regions around bright emissive sources before applying the matched filters to the maps. These sources are detected in the 150 GHz data using a matched filter designed to optimize the S/N of point sources. Masks of $4'$ radius are placed over sources detected at $>5\sigma$, and candidates detected within $8'$ of these sources are excluded from the final cluster lists. Additionally, as referenced above in Section 2.2, there are three extended sources in these fields (NGC 55, NGC 253, and NGC 7293; Dreyer 1888) and one exceptionally bright quasar (QSO B0521–365; e.g., Planck Collaboration et al. 2018) that require additional masking. Masks of radius $0\fdg33$ are used for the NGC sources and radius $0\fdg25$ for the quasar. Regions around these sources are also inspected following the cluster filtering process, and a small number of spurious candidates are rejected. In total 122 deg^2 are masked, 4.5% of the full survey area.

3.3. Candidate Identification

Cluster candidates are identified as peaks in the matched-filtered maps. For each location we define our SZ observable, ξ, as the maximum detection significance over the 12 filter scales.

---

[86] Given the arcminute scale beam, essentially all extragalactic sources at $z > 0.05$ are unresolved in SPT data. See, e.g., discussion of such sources in the SPT-SZ survey in W. Everett et al. (2020, in preparation).

[87] From 1.5 to 3 air masses as compared to the median air mass of ~1.2 for the SPTpol main survey field.

---

[88] Though see, e.g., Wright (1979), Nozawa et al. (2000), Itoh & Nozawa (2004), and Chluba et al. (2012) for discussion of relativistic corrections that become relevant at $T_{\mathrm{e}} \gtrsim 8$ keV.

As in prior SPT analyses, there is a small decl. dependence in the noise owing to atmospheric loading, detector responsivity, and coverage changes across each field. To capture this in the ξ estimates, each filtered map is split into $90'$ strips in decl. and —as in Huang et al. (2019)—noise in each strip is measured by measuring the standard deviation of a Gaussian fit to unmasked pixels. In this work, all candidates $\xi \geqslant 5$ are reported, and for $4 < \xi < 5$, where our follow-up is currently highly spatially incomplete, we also report confirmed systems in the DES common region (see Section 4).

3.4. Field Depth Scaling and False Detection Rate

We make use of simulations to estimate the contamination of our catalogs by spurious detections and to renormalize the measured SZ detection significances to account for the varying field depths (see Section 5.1.1). Simulations were previously used to this effect in, e.g., Reichardt et al. (2013), de Haan et al. (2016), and Huang et al. (2019); we briefly overview the process here and describe some small changes to the process from the SPT-SZ simulations. For more details on these simulations see Huang et al. (2019).

For each field we construct sets of simulated millimeter-wave skies consisting of the following:

1. Primary lensed CMB (Keisler et al. 2011).
2. Signals from Poisson and clustered dusty sources that we approximate as Gaussian random fields with amplitude and spectral indices matching George et al. (2015).
3. Discrete radio sources below the masking threshold with the source population drawn from the model of De Zotti et al. (2005) and with spectral indices drawn from the results of George et al. (2015) and Mocanu et al. (2013).
4. Thermal SZ constructed using a halo light cone from the Outer Rim (Habib et al. 2016; Heitmann et al. 2019) simulation with thermal SZ profiles painted for each halo with $M_{200c} > 10^{13}$ following the methodology of Flender et al. (2016) and using the pressure profiles of Battaglia et al. (2012). The thermal SZ power is consistent with the results of George et al. (2015). The SZ signal is omitted in the false detection simulations.
5. Atmospheric and instrumental noise from jackknife noise maps constructed via co-adding field observations where half of the observations were randomly multiplied by -1.

Each sky realization is convolved with the SPT beam and transfer function. As in Huang et al. (2019), there are two significant changes compared to simulations used for SPT-SZ cluster studies. First, we use discrete radio sources, as opposed to Gaussian random fields, to account for radio contamination. This change was found to be important for properly capturing the false detection rates of the deeper SPTpol 100d and 500d cluster surveys but has negligible impact at the noise levels of the SPT-ECS and SPT-SZ surveys. We adopt it for consistency here. Second, we use the measured SPT beams, as opposed to Gaussian approximations, which enables more consistent scalings between the SPT-SZ and SPTpol experiments.

To estimate the number of spurious detections in each field, we run the cluster detection algorithm on the simulated SZ-free maps. As in de Haan et al. (2016), to reduce shot noise in our estimates from our finite number of simulations, we model the

false detection rate with the function

$$N_{\text{false}}(>\xi) = \alpha_{\text{field}} e^{-\beta_{\text{field}}(\xi-5)} \times \text{field area.} \quad (3)$$

All of the fields are well approximated by $\alpha \sim 0.008$ and $\beta = 4.3$; as each field is approximately 260 deg^2, this results in ~ 2 false detections per field expected above $\xi = 5$ and 17–18 above $\xi = 4.5$.

As detailed in de Haan et al. (2016), the field depth rescaling factors, which track changes in "unbiased significance" as a function of mass for the varying field depths, are determined by measuring the S/N of simulated clusters at their known locations and optimal filter scales from the simulated maps (see also Section 5.1.1). We list the field depth rescaling factors γ_{field} in Table 1. Following previous SPT publications, the absolute normalization is set to correspond to the unit scaling adopted in Reichardt et al. (2013). While in principle the field scaling simulations should be sufficient to properly scale the SPT-ECS field depths relative to SPT-SZ, the extra calibration steps required for the SPT-ECS survey make this challenging. To capture any residual uncertainty in this process, we introduce a new parameter, γ_{ECS}, which rescales all field scalings in the SPT-ECS survey $\gamma_{\text{SPT-ECS},i} = \gamma_{\text{ECS}} \times \gamma_{\text{field},i}$. With this parameterization, $\gamma_{\text{ECS}} = 1$ means that our simulations capture the entirety of the relative difference in effective depth between SPT-SZ and SPT-ECS. We empirically calibrate γ_{ECS} in Sections 5.1.2 and 6.1.

3.5. Potential Contamination of the SZ Sample from Cluster Member Emission

Galaxy clusters contain an overdensity of galaxies relative to the field, and galaxies emit radiation at millimeter wavelengths. Since the thermal SZ signal from the cluster gas is a decrement in the frequency bands used in this work, any positive emission above the background will act as a negative bias to the SZ signature. We can classify the potential bias from cluster galaxy emission into two regimes, one in which the integrated emission from many cluster members produces an average bias to all clusters in a given mass and redshift range, with little variation from cluster to cluster, and one in which a single bright galaxy (or a very small number of bright galaxies) imparts a significant bias to a random subsample of clusters. We can also separate the contributions to this effect from the two primary classes of millimeter-wave-emissive sources: active galactic nuclei producing synchrotron emission ("radio sources") and star-forming galaxies producing thermal dust emission ("dusty sources").

The contribution to the second type of bias from dusty sources is expected to be negligible, because the dusty source population falls off steeply at high flux (e.g., Mocanu et al. 2013), so that the areal density of dusty sources bright enough to fill in a cluster decrement at a level important for this work is very low. This statement is for the field galaxy population, so if galaxies in clusters were more likely than field galaxies to be dusty and star-forming, the bright population could still be an issue. In fact, the opposite is expected to be true, i.e., compared to the field population, galaxies in clusters are less likely to be dusty and star-forming, at least at $z < 1$ (e.g., Bai et al. 2007; Brodwin et al. 2013; Alberts et al. 2016). In Vanderlinde et al. (2010), it was argued that the other regime of bias from dusty sources is also negligible for clusters more massive than $\sim 2 \times 10^{14} M_\odot$, which includes all the clusters in this sample (see also, e.g., Soergel et al. 2017 for an analysis of a sample of

low-z optically selected clusters, and Erler et al. 2018; Melin et al. 2018 for explorations of the *Planck* sample).

To assess the potential contamination from radio sources, we make use of the publicly available maps from the 1.4 GHz National Radio Astronomy Observatory Very Large Array (VLA) Sky Survey (NVSS; Condon et al. 1998).[89] NVSS covers the full sky north of decl. $-40°$ and thus has nearly 100% overlap with the survey fields in this work. The data for the NVSS were taken between 1993 and 1997, so source variability will limit the fidelity of the estimate of contamination to any individual cluster, but we can make some statements about the average or median contamination across the catalog and the fraction of clusters expected to be strongly affected by radio source contamination.

For each of our survey fields, we download all NVSS postage-stamp maps (each $4° × 4°$) that have any overlap with that field and reproject them onto the same pixel grid as used in our cluster analysis. We then make beam- and transfer-function-matched NVSS maps for each of the SPTpol observing frequencies by convolving the NVSS maps with a kernel defined by the Fourier-space ratio of the SPTpol beam and transfer function at that frequency and the effective NVSS beam (a $45''$ FWHM Gaussian). We scale the intensity in these maps from 1.4 GHz to SPTpol frequencies assuming a spectral index of -0.7 (roughly the mean value found for radio sources in clusters by Coble et al. 2003), and we convert the result to CMB fluctuation temperature.

We then combine the SPTpol-matched NVSS maps in our two bands using the same band weights as used in the cluster-finding process (Section 3) and filter the output with the same β-model-matched filters as used in the cluster-finding process. For each cluster candidate in the catalog, we take the combined NVSS map filtered with the same β-model profile as the cluster candidate, and we record the value of the combined, filtered NVSS map at the candidate location. We divide that value by the same noise value used in the denominator of the ξ value for the cluster candidate, and we record that value as our best estimate of the contamination to the ξ value of that cluster candidate from radio sources. Since the NVSS maps contain all the radio flux at 1.4 GHz (not just the sources bright enough to be included in the NVSS catalog), this test accounts for both regimes of bias discussed above.

The median contamination calculated in this way is $\Delta \xi_{med} = -0.05$, or 1% of the threshold value for inclusion in the catalog of $\xi = 5$. Of the 266 candidates in the catalog, 13 ($\sim$5%) have a predicted contamination of greater than 10% of their measured SZ flux, and 7 ($\sim$2.6%) have a predicted contamination of greater than 20%. One cluster candidate, SPT-CL J2357-3446, has an anomalously large predicted bias of $\Delta \xi = -11.1$. This candidate is almost certainly the low-redshift ($z = 0.048$) cluster A3068 (separation $0\rlap{.}'1$), and it is within $0\rlap{.}'6$ of the NVSS source NVSS J235700$-$344531, which has a catalog 1.4 GHz flux of 1.28 Jy. This NVSS source is a cross-identification of PKS 2354$-$35, which lies at a redshift consistent with being a member of A3068 ($z = 0.049$) and is identified as the central galaxy of this cluster by many authors (e.g., Schwartz et al. 1991). Given the relative redshift dependence of the thermal SZ signature of clusters and the flux density of member emission, it is not surprising that the highest level of radio source contamination occurs in one of the lowest-

redshift clusters in the sample. It is somewhat surprising, though, that a cluster with a predicted radio source contamination of $\Delta \xi > 10$ would be detected at $\xi = 5.5$, as this one is in our catalog. The apparent answer to this puzzle is source variability. More recent observations of this source with the Australia Compact Telescope Array (ATCA) at 5 GHz (Burgess & Hunstead 2006) resulted in a measured flux density of 99 mJy, which would imply a spectral index of < -2.0 if naively combined with the NVSS measurement at 1.4 GHz. We conclude that during our observations the 150 GHz flux of this source was likely <10 mJy (as implied by the ATCA measurement and a spectral index of -0.7) rather than the $\sim$50 mJy implied by the NVSS measurement. Finally, we also note that all previous SPT cluster cosmology results have cut clusters below $z = 0.3$ or 0.25, so this cluster would not normally be included in an SPT cosmology analysis.

These contamination numbers will be diluted somewhat by any false detections. However, removing the 22 unconfirmed candidates at $\xi > 5$ has a negligible effect. If we extend the sample to all confirmed systems at $\xi > 4$ (for a total of 448 clusters), we find a similar median contamination ($\Delta \xi_{med} = -0.050$) and fraction of systems above a given level of contamination: 17 ($\sim$4%) and 8 ($\sim$2%) above 10% and 20% contamination, respectively. We flag candidates with >10% potential contamination of their measured SZ signal in Tables 8 and 9.

3.6. Clusters in Masked Regions

In addition to the potential bias to our sample from the millimeter-wave emission from cluster members, there is a potential bias from the avoidance of millimeter-wave-bright sources in our cluster finding. As discussed in Section 3.2, we discard any cluster detection within $8'$ of a source detected at 5σ ($\sim$9–15 mJy, field dependent) at 150 GHz. If there were a strong physical association between galaxy clusters and such sources, our measured cluster abundance would be biased low.

The majority of sources with 150 GHz flux density above 9 mJy are flat-spectrum quasars (see, e.g., Mocanu et al. 2013; Gralla et al. 2019), and, based on studies of radio galaxies from lower-frequency surveys (e.g., Lin et al. 2009; Gralla et al. 2011, 2014; Gupta et al. 2017), there is not expected to be a significant SZ selection bias from these sources. However, we can perform several checks on the effects of masking with the data in hand. First, as in B15, we perform a secondary cluster search, this time only masking emissive sources detected at >100 mJy at 150 GHz. Each candidate from this run was visually inspected, and, as expected, this candidate list was dominated by filtering artifacts; no new clusters were identified in this secondary run.

We also check for any statistical association between the flux-limited DES redMaPPer optically selected cluster catalog and associated random locations (discussed in more detail below in Section 4.1.1 and in Rykoff et al. 2016) and SPT-selected emissive sources. To increase the sensitivity of this test, we also include sources from the SPT-SZ survey, which had a 5σ source threshold of lower flux ($\sim$6 mJy; W. Everett et al. 2020, in preparation). We first measure the probability of optical clusters and random locations to be within the $8'$ source masks and find marginal differences between the two. Adopting a $3'$ radius to reduce the noise from chance associations and further restricting the cluster sample to $z > 0.25$ where we expect the SPT selection to be well

---

[89] Maps downloaded via anonymous ftp from https://www.cv.nrao.edu/nvss/postage.shtml.

Table 2
Optical Clusters near Millimeter-wave-bright Sources

λ Range	N_{clusters}	% in Masked Region	$N_{\text{clusters}}^{\text{SPT-SZ}}$	%
Randoms	2.1e6	0.9	1.2e6	1.05
20–30	2.3e4	1.11	1.3e4	1.4
30–50	9.3e3	0.95	5.4e3	1.1
50–80	1.9e3	1.22	1.1e3	1.65
>80	3.5e2	1.13	2.0e2	1.5

Note. Percentage of DES redMaPPer clusters at $z > 0.25$ that fall within $3'$ of bright emissive sources; N_{clusters} corresponds to the total number of clusters in a given richness bin within the SPT-SZ+SPT-ECS (left) or SPT-SZ only (right) footprint. The top row provides statistics for random sources. Less than 1% of clusters over random fall in the masked areas.

understood, we find an excess probability over random of $\lesssim 1\%$ for clusters to fall in the source-masked regions (see Table 2). While the purity of the flux-limited sample is expected to decrease at high redshift (thus limiting our ability to test for trends with redshift), we note that we find no significant difference in the fraction of clusters in masked regions between the full sample and two subsamples constructed by splitting the optical sample at its median redshift of $z = 0.755$.

4. External Data Sets and Cluster Confirmation

To confirm the SZ candidates as galaxy clusters, we make use of targeted optical and NIR follow-up observations, data drawn from the wide-area DES (Flaugher et al. 2015), the Pan-STARRS1 survey (Chambers et al. 2016), the all sky *Wide-field Infrared Survey Explorer* (*WISE*) data set (Wright et al. 2010), and the literature. In this section we describe each data set and how it is used to confirm and/or characterize the SZ-selected clusters. Overall, we focus our targeted follow-up efforts on ensuring nearly complete imaging of high-significance ($\xi > 5$) cluster candidates to depths sufficient to confirm clusters to $z \sim 0.8$–1.0. For lower-significance targets we rely significantly more on the availability of wide-area imaging data sets.

4.1. External Data Sets

4.1.1. The Dark Energy Survey and redMaPPer

The DES is a recently completed ~ 5000 deg^2 optical–NIR imaging survey conducted with the DECam imager (Flaugher et al. 2015) on the 4 m Blanco Telescope at Cerro Tololo Inter-American Observatory. The survey was designed to have significant overlap with the original SPT-SZ survey (see Figure 1), and we have increased this overlap with the addition of SPT-ECS. In this work we make use of the DES data acquired in Years 1–3 of the survey; these data reach an S/N of 10 in $1''95$ apertures in the $grizY$ bands at [24.33, 24.08, 23.44, 22.69, 21.44] mag with resolution—given by the median FWHM of the point-spread functions—of [1.12, 0.96, 0.88, 0.84, 0.9] arcseconds, respectively (Abbott et al. 2018).[90]

We make particular use of the redMaPPer optically selected galaxy cluster sample drawn from the DES data. As its name implies, redMaPPer (hereafter RM) is a red-sequence-based cluster finder that identifies clusters as overdensities of red galaxies based on galaxy positions, colors, and brightness

(Rykoff et al. 2014, 2016). Each RM cluster detection provides —among other quantities—a cluster redshift, a probabilistic center (based on the consistency of bright cluster members with the observed properties of cluster central galaxies), a similarly probabilistic cluster member catalog, and a total optical richness, λ, that is the sum of all the cluster member probabilities corrected for various masking and completeness effects. The RM sample has been shown to have excellent redshift precision, with uncertainties in redshift estimates of $\sigma_z/(1 + z) \sim 0.01$ for clusters $z < 0.9$.

There are two different RM catalogs: a "flux-limited" sample that includes significant numbers of high-redshift clusters for which the optical richness estimates must be extrapolated, and a "volume-limited" sample for which the DES data are sufficiently uniform and deep that the richnesses can be well measured; DES cluster cosmology constraints are derived using the volume-limited sample (Rykoff et al. 2016; McClintock et al. 2019). In this work, we explore characteristics of the joint SPT-RM cluster sample using the volume-limited catalog.[91] In total there are 53,610 (21,092) RM clusters at $\lambda > 20$ in the full (volume-limited) DES sample, with $\sim 36,000$ ($\sim 16,000$) and $\sim 14,000$ (~ 6000) of these clusters within the total SPT and SPT-ECS survey area, respectively.

4.1.2. The Parallel Imager for Southern Cosmology Observations

We use the Parallel Imager for Southern Cosmology Observations (PISCO; Stalder et al. 2014)—a new imager with a $9'$ field of view installed on the 6.5 m Magellan/Clay telescope at Las Campanas Observatory in Chile—to obtain approximately uniform depth $griz'$ imaging data for over 500 SPT-selected clusters and cluster candidates, including 173 candidates at $\xi \geqslant 4.5$ in SPT-ECS. These data were obtained as part of an ongoing effort to characterize the strong-lensing and bright galaxy populations of the SPT cluster sample.

To analyze the PISCO data, we have constructed a reduction pipeline that includes standard corrections (i.e., overscan, debiasing, flat-fielding, illumination, though we note that defringing is not required), as well as specialized routines that correct the data for nonlinearities and artifacts caused by bright stars. After the images have been flat-fielded, we use the PHOTPIPE pipeline (Rest et al. 2005; Garg et al. 2007; Miknaitis et al. 2007) for both astrometric and relative calibration prior to co-addition. We make use of stars from the DES DR1 public release (Dark Energy Survey Collaboration et al. 2018), from the second *Gaia* data release (Gaia Collaboration et al. 2018), or from the Pan-STARRS1 release (Flewelling et al. 2016) to obtain sufficient numbers of sources for good astrometric solutions. Images are co-added using SWarp (Bertin et al. 2002), and sources are detected in the co-added images using SExtractor (Bertin & Arnouts 1996) in dual-image mode with the r-band image set as the detection image. We find the typical $\sim 85\%$ completeness depth of these images to be $r = 24.3$. We separate bright stars and galaxies using the *SG* statistic (Bleem et al. 2015a) and use these stars to calibrate the photometry with stellar locus regression (High et al. 2009); absolute magnitudes are set using the Two Micron All Sky Survey (2MASS) point-source catalog (Skrutskie et al. 2006).

---

[90] Data available: https://des.ncsa.illinois.edu/releases/dr1.

[91] RM catalog version 6.4.22.

4.1.3. Spitzer/IRAC and Magellan/Fourstar

Based on initial PISCO imaging, we were able to identify a small number of high-redshift cluster candidates worthy of additional follow-up observations. Two systems were imaged as part of a *Spitzer* Cycle 11 program, and five additional SPT-ECS cluster candidates were part of a Cycle 14 program (ID: 11096,14096; PI: Bleem).[92] The Cycle 11 (14) candidates were observed with *Spitzer*/IRAC (Fazio et al. 2004) for 360 (180) s on source integration time in both the 3.6 and 4.5 μm bands. These data were reduced as in Ashby et al. (2009) and are of sufficient depth for cluster confirmation to $z \sim 1.5$.

We have additionally obtained ground-based NIR *J*-band imaging for 19 candidates with the Fourstar imager (Persson et al. 2013) installed on the Magellan/Baade telescope. For each candidate, a large number of short exposures were taken using predefined dither macros provided in the instrument control software with the candidate centered on one of the four Fourstar detectors. These images were flat-fielded using IRAF routines (Tody 1993), astrometrically registered and relatively calibrated, and co-added using the PHOTPIPE pipeline. Co-addition was performed with SWarp and source identification with SExtractor. Absolute calibration is tied to the *J*-band flux from stars in the 2MASS point-source catalog. While conditions varied between the Fourstar observations, these data are typically sufficient to confirm clusters to $z \sim 1.2$ or better.

4.1.4. Pan-STARRS1

The SPT fields north of $\delta = -30°$ have been imaged by the Panoramic Survey Telescope and Rapid Response System (Pan-STARRS) in the $grizy_p$ filter bands as part of the Pan-STARRS 3π Steradian Survey (Chambers et al. 2016). In this work we make use of the first data release (Flewelling et al. 2016) available for download from the Mikulski Archive for Space Telescopes.[93] This data release contains images and source catalogs from the "stack" co-added image products. These data are shallower than both the DES survey data and our targeted follow-up imaging, with 5σ point-source depths of [23.3, 23.2, 23.1, 22.3, 21.4] mag in the $grizy_p$ bands, respectively. Exploring the properties of clusters in the Pan-STARRS footprint that we confirmed in DES, PISCO, and the literature (see below), we find that the Pan-STARRS data typically enable robust confirmation of clusters to $z < 0.6$–0.7.

4.1.5. WISE

As demonstrated in, e.g., Gonzalez et al. (2019), observations from *WISE* (Wright et al. 2010) are an excellent resource for identifying high-redshift clusters. Of particular relevance for this work are the observations in the [*W*1] and [*W*2] filter bands at 3.4 and 4.6 μm, which we use to confirm cluster candidates by identifying overdensities of high-redshift galaxies at a common 1.6 μm rest frame (see, e.g., Muzzin et al. 2013). Here we make use of "unWISE," a new processing of *WISE* and NEOWISE (Mainzer et al. 2014) data that reaches 3 times the depth of the AllWISE data (Meisner et al. 2017; Schlafly et al. 2019).[94]
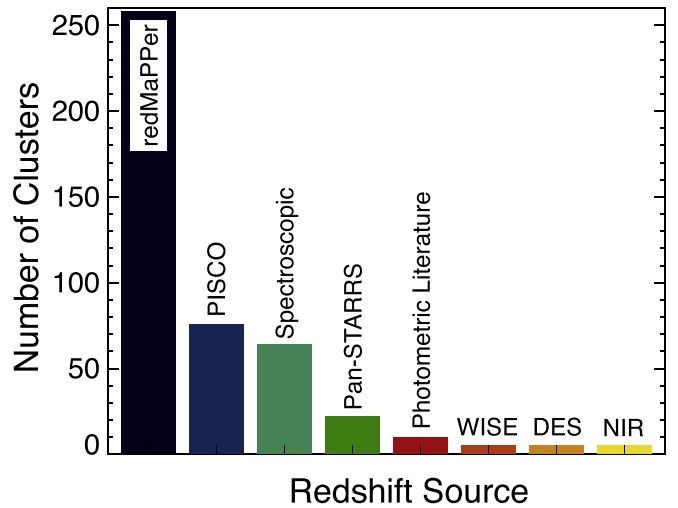
Figure 2. Distribution of the telescope/surveys used to confirm and provide redshifts for the SPT clusters presented in this catalog. While some clusters may have redshifts from multiple sources (e.g., there is significant overlap between PISCO and RM), we only represent each cluster once in this figure, highlighting the sources of the redshifts reported in Tables 8 and 9. The DES column corresponds to clusters with redshifts from DES data but not from RM (see Section 4.2.2). Generally, data from Pan-STARRS are deep enough to confirm clusters to $z \sim 0.6$, DES and PISCO to $z \sim 0.8$–1.0, FourStar to $z \sim 1.2$, and *Spitzer* to $z \sim 1.5$.

4.1.6. Literature Search

We additionally search the literature for known clusters in the vicinity of the SZ-selected candidates. Using the SIM-BAD[95] database, we search for systems within a $5'$ radius of the candidate locations. When such a system is found, we consider it to be a match if it is at $z < 0.3$; we reduce the matching radius to $2'$ for clusters at higher redshifts (except for systems in the *Planck* catalog; see Section 5.3 below). When available, we adopt reported spectroscopic redshifts as the SPT cluster redshifts for previously identified systems. We also make use of reported photometric redshifts for a small number of systems not in DES, Pan-STARRS1, or directly targeted in our follow-up imaging. When possible we use the other external data sets to identify spurious associations with previously reported systems, finding several in this distance-based match.
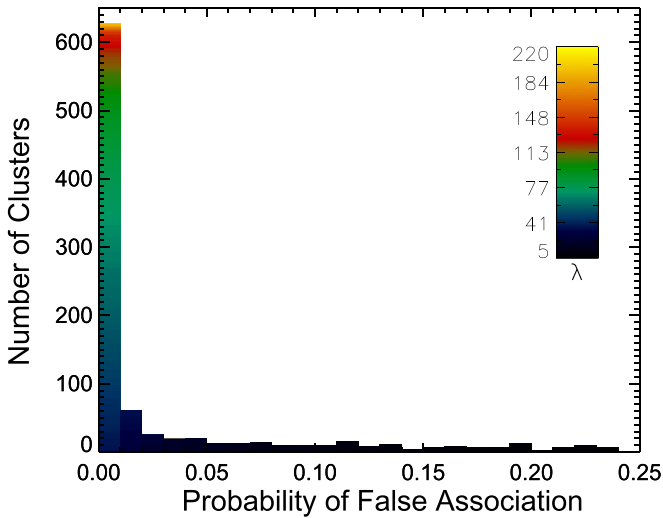
4.2. Cluster Confirmation

We adopt two different techniques for confirming candidates in clusters: a probabilistic matching to RM clusters in the common overlap region and, for candidates outside the volume probed by RM cluster finding on DES data, the identification of significant overdensities of red sequence or 1.6 μm rest-frame galaxies at the locations of cluster candidates using the techniques described in B15. We show the distribution of the origins of SPT-ECS cluster redshifts in Figure 2.

4.2.1. Confirmation with redMaPPer in Scanning Mode

The RM catalog makes strict cuts on sky coverage and photometric depth to ensure a well-understood optical selection function. In the case of matching to an SZ-selected sample, we

---

[92] Data available: https://sha.ipac.caltech.edu/applications/Spitzer/SHA/.
[93] http://panstarrs.stsci.edu/
[94] Data available: http://unwise.me/imgsearch/.
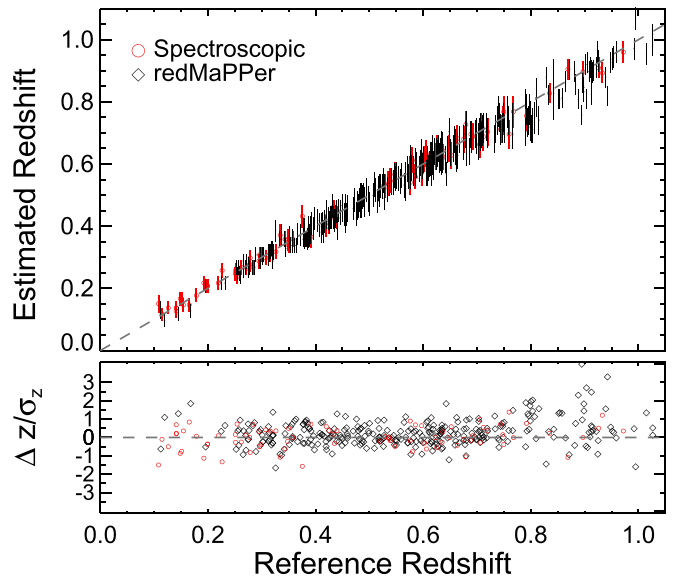[95] http://simbad.u-strasbg.fr/simbad

Figure 3. Distribution of probabilities of false association between redMaPPer targeted confirmations and SPT clusters from the SPT-ECS and SPT-SZ surveys. The color scaling represents the optical richnesses of the RM detections centered on SPT locations. For the purposes of this work we reject associations with probabilities of false association greater than 5%.

Figure 4. Top panel: comparison of estimated red sequence redshifts from PISCO imaging data to spectroscopically measured redshifts (81 systems; red) and redshifts estimated by the redMaPPer scanning-mode algorithm (318 systems; black). Bottom panel: distribution of residuals over the redshift uncertainties; for the RM-PISCO comparison we add the individual uncertainties in quadrature. In general, we find excellent agreement between the redshifts measured from PISCO and both the RM and spectroscopic samples below $z \sim 0.75$.

can somewhat relax these criteria to also enable targeted searches for red sequence galaxy counterparts in regions excluded by these cuts. We have run the RM algorithm in "scanning mode" centered on the SPT location, where the likelihood of a red sequence overdensity in apertures of 500 kpc radius is computed as a function of redshift from $z = 0.1$ to 0.95 in steps of $\delta_z = 0.005$. At each redshift the optical richness is computed at both the SZ location and the most likely optical center; for systems with significant red sequence overdensities the richness and redshift are refined at the highest likelihood redshift using the standard RM radius/richness scaling. Richnesses are recorded for each location where $\lambda \geqslant 5$. We repeat this scanning procedure for 100 mock SZ samples (at over 100,000 sky locations) to compute the probability over random of finding a cluster of richness λ at an SZ location. We report as "confirmed" clusters for which the probability of random association is less than 5%, which corresponds to $\lambda > 19.3$. As this probability distribution is a continuum (with no clear breaks), this choice is somewhat arbitrary; setting this threshold at 0.05 leads to an expectation of <2 false associations in the RM-confirmed sample. In Figure 3 we plot the distribution of matched clusters against the probability of random associations for SPT-SZ ($\xi > 4.5$) and SPT-ECS clusters ($\xi > 4$).

For cluster candidates in the common region not confirmed via the RM scanning-mode process we make use of both DES and *WISE* imaging and photometric catalogs at the cluster locations and, where available, pointed follow-up imaging as described in the next subsection. The confirmation of these clusters follows a similar process to that described below.

4.2.2. Cluster Confirmation from Other Imaging Data Sets

Here we describe the techniques used for confirming cluster candidates not confirmed via the RM algorithm or literature search. We obtained imaging for $\sim$100 candidates outside of the volume searched by RM, as well as some imaging redundant to the DES imaging (in terms of confirmation), as part of our strong-lensing search program that we use here for

redshift comparisons. In total, 173 candidates were imaged with Magellan/PISCO (about 2/3 in common with RM; see Figure 4), 19 with Magellan/Fourstar, and 7 with *Spitzer* (note that the NIR imaging overlaps areas with optical imaging). Ten candidates are located in the DES footprint but are either at high redshift or missing photometry in filters required for RM, and 22 candidates only fall in the Pan-STARRS footprint.

To conduct our targeted search for red sequence galaxies in these areas, we first calibrate our synthetic model for the colors and magnitudes of red sequence galaxies, generated with the GALAXEV package (Bruzual & Charlot 2003) by assuming a passively evolving stellar population with single formation burst at $z = 3$, to match the relevant survey photometry using samples of known clusters with spectroscopic redshifts. For PISCO, the data set that we most use to confirm clusters outside of DES, we use 58 SPT-SZ galaxy clusters with spectroscopic redshifts that were imaged as part of our broader SPT characterization program. In Figure 4 we plot in red the measured PISCO redshifts versus those from the training sample, as well as additional SPT-ECS clusters with spectroscopic redshifts reported in the literature. The typical redshift precision is $\sigma_z/(1 + z) \sim 0.015$, with uncertainties increasing toward higher redshifts. We also plot in black the PISCO redshifts compared to those from the DES RM catalog for 318 systems in SPT-SZ and SPT-ECS and find generally good agreement between the two, though the comparison suggests that the redshifts estimated from PISCO may tend be underestimated at the highest redshifts. More spectroscopic data on high-redshift clusters from ongoing SPT programs will help further validate/improve the PISCO redshift calibration for such systems. Given the excellent redshift precision of the RM algorithm, we adopt RM scanning-mode redshifts by default when clusters are confirmed by both methods. We repeat a similar process with DES photometry, finding $\sigma_z/(1 + z) \sim 0.015$, and with 35 spectroscopic clusters (as identified in the SPT-ECS literature

search) at $0.108 < z < 0.72$ in the Pan-STARRS1 footprint, finding $\sigma_z/(1 + z) \sim 0.03$ in these shallower data.

We search the optical/NIR imaging for an excess of red sequence galaxies (or alternatively 1.6 μm rest-frame galaxies in the case of *Spitzer* and *WISE* confirmations) in the vicinity (2′–3′) of the SPT cluster candidates. We call a cluster "confirmed" when significant excesses of these galaxies over background are identified (see, e.g., B15 for more details on the confirmation procedure). In Song et al. (2012) we estimated that <4% of cluster candidates identified via this procedure would be false associations, and for clusters in common between the PISCO and DES imaging, we can cross-check our assigned confirmations against the statistical process described in Section 4.1.1. We note that this is of course a lower limit to the false association rate, as the DES data are also of finite redshift reach. In this comparison we find that ∼1% (3/318) of candidates with RM cluster matches that were also targeted with PISCO were assigned a different cluster counterpart when using the PISCO data. In two circumstances the PISCO data were insufficiently deep to correctly confirm the higher-redshift ($z \sim 0.9$) clusters, while the remaining system was a super-position of two rich clusters ($\lambda = 75$ and $\lambda = 65$) for which the targeted RM algorithm selected the lower-redshift system as the richer cluster and the PISCO data the higher.

For confirming higher-redshift systems without targeted *Spitzer* or Magellan/Fourstar data we combine data from "unWISE" with optical source catalogs. Following Gonzalez et al. (2019), we adopt a 1″5 matching radius to associate *WISE* sources with optical galaxies and exclude sources with $i < 21.3$ and $W1$–$W2 < 0.2$, as these cuts were found to remove low-redshift ($z < 0.8$) galaxies. Similar to the analysis of clusters with *Spitzer* imaging, we search for a local excess of galaxies at 1.6 μm rest frame in the vicinity of the SPT cluster candidates. We validated this search process on clusters from the SPT-SZ sample (B15; Khullar et al. 2019) with spectro-scopic redshifts $z > 0.85$, finding that we were able to robustly confirm 20/23 of these systems. From this spectroscopic sample we were able to quantify the redshift uncertainty in our *WISE* measurements as $\sigma_z/(1 + z) \sim 0.1$. Improving this redshift precision via more sophisticated catalog cuts and photometric analysis of the *WISE* data is work in progress.

4.2.3. 2dFLenS

The 2dFLenS survey (Blake et al. 2016) targeted luminous red galaxies (LRGs) at $z < 0.9$ with a primary focus on measuring redshift-space distortions and—in combination with KiDS survey data—galaxy–galaxy lensing (Joudaki et al. 2018) and the characterization of redshift distributions via cross-correlation (Johnson et al. 2017). There is significant overlap between the southern field of 2dFLenS and SPT-ECS. A number of visually identified brightest cluster galaxies (BCGs) from SPT clusters were targeted in a spare-fiber program (though all but two were lost owing to weather), and here we identify additional 2dFLenS sources associated with SPT clusters. First, for each confirmed candidate in the SPT sample at $z < 0.9$, we search for spectroscopic LRGs within 2′.5 of the cluster location and find 47 systems with spectroscopic galaxy associations. Repeating the process on the 40 random position catalogs provided by the 2dFLenS team,[96] we find an average of 17 such matches per mock

---

[96] http://2dFLens.swin.edu.au/

catalog, resulting in ∼30 matches over random for the real data sample. We further improve the purity of the matching by restricting matched galaxies to have redshifts within 2σ of the photometric redshift error (or $\delta z < 0.015$ for clusters with spectroscopic redshifts) and find 39 clusters with spectroscopic galaxy counterparts, including two systems that were targeted as part of the spare-fiber program, compared to an average of two systems for the random catalogs. We list these systems in Appendix B in Table 7.
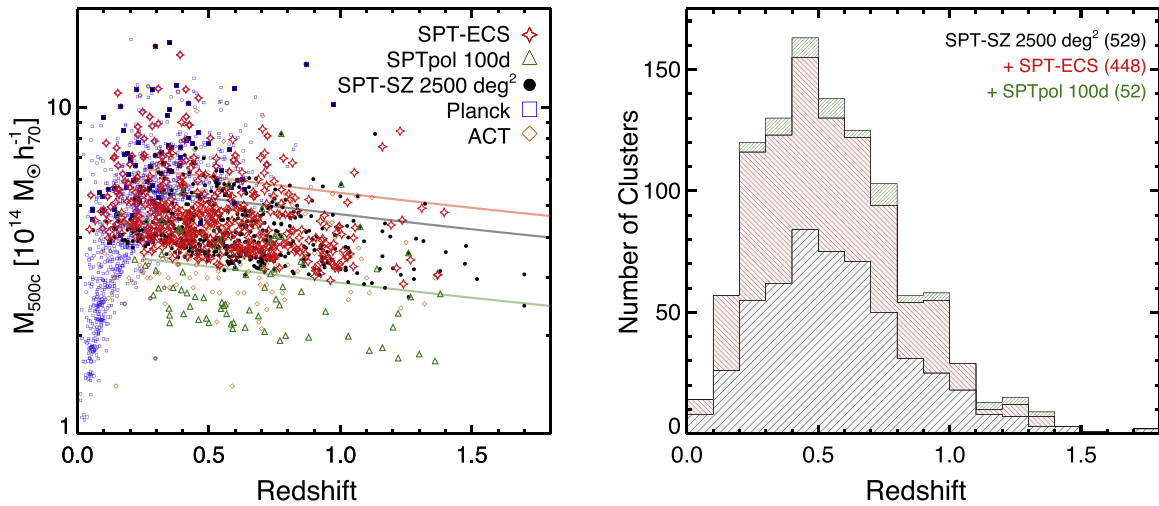
5. The Cluster Sample

In this section we describe the new SZ-selected cluster sample. We also compare the properties of these clusters to those of SZ-selected clusters identified by *Planck* in the SPT-ECS region. Using the confirmation criteria presented in Section 4, we confirm 244 of 266 candidates at $\xi \geqslant 5$. We also leverage the DES and other imaging data to confirm an additional 204 clusters at $4 < \xi < 5$ but note that while the DES imaging is sufficient for cluster confirmation out to $z \sim 0.8$–1.0 in the SPT-ECS-DES overlap region, our follow-up of this lower-significance sample is otherwise highly incomplete.

While the confirmation process is still ongoing, we can compare these numbers to our expected numbers of false detections as estimated in Section 3.4. As discussed in B15, expectations from simulations were found to be in good agreement with observations of the more uniformly and deeply imaged SPT-SZ sample. At $\xi \geqslant 5$, where our optical follow-up imaging is sufficient to confirm clusters to at least $z \sim 0.85$, we find 22 unconfirmed candidates compared to the expected 21 ± 4. This places an empirical lower limit on the purity of 91% for the $\xi > 5$ SZ candidate sample, which, when compared to the simulation prediction, suggests that there are relatively few clusters that remain to be confirmed. For the $\xi \geqslant 4.5$ SZ candidate sample, where the follow-up is generally more heterogeneous/incomplete, we find 180 currently uncon-firmed candidates compared to 174 ± 13 expected, resulting in a lower limit to the purity of 64%.

The confirmed cluster candidates have a median redshift of $z = 0.49$ and median mass (calculated as described below in Section 5.1.1) of $M_{500c} \sim 4.4 \times 10^{14} M_\odot \, h^{-1}$. Twenty-one of the systems are at $z > 1$, bringing the total number of $z > 1$ systems from SPT-SZ, SPTpol 100d (Huang et al. 2019), and SPT-ECS to over 75 out of >1000 confirmed systems. The mass and redshift distribution of the cluster sample as compared to other SZ-selected samples, as well as a histogram of the redshift distribution of the SPT samples, is shown in Figure 5. We note that, given the lack of deep NIR data redder than z band, the RM algorithm can systematically under-estimate redshifts at $z > 0.9$, which may be the source of the small gap in the cluster redshift distribution at $z \sim 1.1$.

In Figure 6, we present an estimate of the survey complete-ness as a function of mass and redshift for our main sample at $\xi > 5$ using the ξ−mass relation (see below in Section 5.2). The survey is on average >90% complete at all redshifts $z > 0.25$ for masses above $M_{500c} \sim 6.5 \times 10^{14} M_\odot \, h^{-1}$ (in comparison to $M_{500c} \sim 5.5 \times 10^{14} M_\odot \, h^{-1}$ for the SPT-SZ survey at the same significance threshold), with the mass at which the survey is 90% complete shifting by less than $1 \times 10^{14} M_\odot \, h^{-1}$ from the mean between the fields. The mass corresponding to a fixed completeness value falls as a function of redshift, with the survey on average 90% complete at $M_{500c} = 5.4 \times 10^{14} M_\odot \, h^{-1}$ at

Figure 5. Left: mass and redshift distribution of the SPT-ECS cluster sample detected at $\xi \geqslant 4$. The median redshift of the sample is $z = 0.49$, and the median mass is $M_{500c} \sim 4.4 \times 10^{14} M_\odot \, h^{-1}$. Overplotted are cluster samples from other SZ surveys, including the 100d SPTpol survey (green triangles; Huang et al. 2019), the 2500d SPT-SZ Survey (black circles; Bleem et al. 2015b, with redshifts updated as in Bocquet et al. 2019), the PSZ2 cluster sample from Planck Collaboration et al. (2016b) (blue squares), and the cluster samples from the ACT Collaboration (orange diamonds; Hasselfield et al. 2013; Hilton et al. 2018). Clusters found in both SPT and other samples are plotted at the SPT mass and redshift and, for clusters in common between other samples, at the mass and redshift at which the cluster was first reported. We also plot at $z > 0.25$, as solid colored lines, the 90% completeness thresholds for $\xi \geqslant 5$ for the three SPT surveys (see also Figure 6). Right: redshift histogram of the three reported SPT cluster surveys. The numbers of clusters in each survey—with each cluster only reported once (so that, e.g., clusters in both SPTpol 100d and SPT-SZ are only counted once)—are listed to the right of each survey name. The contribution from the SPTpol 100d survey is plotted on top in the green right-diagonal-hashed region, the contribution from the SPT-ECS survey is plotted in the red left-diagonal-hashed region, and the contribution to the total from the SPT-SZ survey is plotted in the black right-diagonal-hashed region. Combined with these other two samples, the SPT-ECS sample brings the number of SZ-detected clusters reported by the SPT collaboration to over 1000.
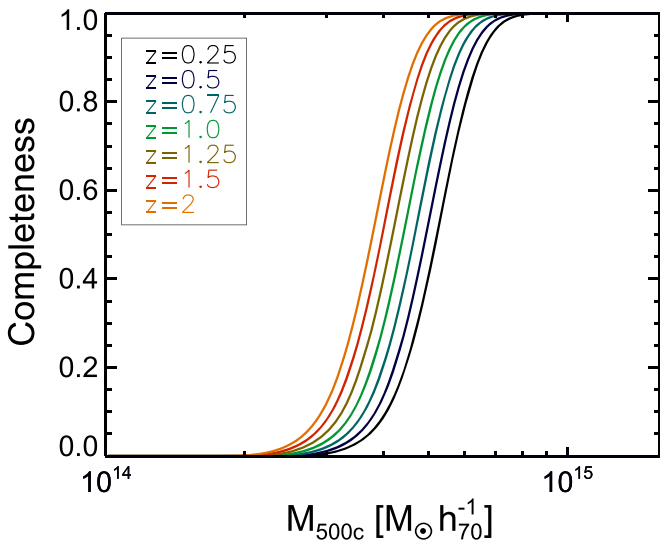
Figure 6. Average (across all fields) completeness as a function of mass and redshift for the SPT-ECS survey at $\xi \geqslant 5$, the ξ threshold for which we provide the complete candidate list for the full survey. The survey is on average 90% complete for all redshifts at $z > 0.25$ for masses above $M_{500c} \sim 6.5 \times 10^{14} M_\odot \, h^{-1}$. This completeness is derived for a fixed cosmology as discussed in Section 5.1.1 and Bocquet et al. (2019).

$z > 1$. In Table 8, we provide a complete listing of the candidates at $\xi \geqslant 5$, including their positions, detection significances, and the filter scales that maximize these significances. For confirmed clusters we also include redshifts, estimated masses, and optical richness measures (where available), and we flag notable properties about the systems. In Table 9 we provide a similar listing for the lower-significance confirmed systems.

As mentioned in Section 4.1.6, we also conducted a literature search for previously identified clusters, finding that 147 SPT-ECS candidates have been previously reported, including a

number of systems in the Abell and *Planck* cluster samples (Abell 1958; Abell et al. 1989; Planck Collaboration et al. 2016b), as well small numbers of systems in other samples (e.g., APM, MACS, SWXCS, MaDCoWS; Dalton et al. 1997; Cavagnolo et al. 2008; Mann & Ebeling 2012; Liu et al. 2015b; Gonzalez et al. 2019). By far the largest overlap is with the *Planck* PSZ2 sample; we explore this in more detail in Section 5.3.

5.1. Comparison to the SPT-SZ Cluster Abundance

The cluster catalog extracted from SPT-ECS should be statistically consistent with the catalog extracted from the SPT-SZ survey once the different survey properties such as depth are accounted for. To test this, we use a cluster number count (NC) analysis to calibrate the parameters of the ξ–mass scaling relation assuming a fixed cosmology and compare the results with those obtained for SPT-SZ.

5.1.1. The SZ ξ–Mass Relation

To connect the observed SZ significance, ξ, to cluster mass, we adopt an observable–mass scaling relation of the form

$$\langle \ln \zeta \rangle = \ln \left[A_{\mathrm{SZ}} \left(\frac{M_{500c}}{3 \times 10^{14} M_\odot \, h^{-1}} \right)^{B_{\mathrm{SZ}}} \left(\frac{H(z)}{H(0.6)} \right)^{C_{\mathrm{SZ}}} \right], \quad (4)$$

$$P(\ln \zeta | M, z) = \mathcal{N}[\langle \ln \zeta \rangle(M, z), \sigma_{\ln \zeta}^2], \quad (5)$$

where A_{SZ} is the normalization, B_{SZ} the slope, C_{SZ} the redshift evolution, $\sigma_{\ln \zeta}$ the lognormal scatter on ζ, and $H(z)$ the Hubble parameter. The variable ζ represents the "unbiased" significance that accounts for the maximization of ξ over position and

filter scales during cluster detection:

$$P(\xi|\zeta) = \mathcal{N}(\sqrt{\zeta^2 + 3}, 1) \qquad (6)$$

for $\zeta > 2$ (Vanderlinde et al. 2010). As in previous SPT publications, we rescale A_{SZ} on a field-by-field basis to account for the variable depth of the survey: $A_{SZ,field} = \gamma_{field} \times A_{SZ}$ (e.g., Reichardt et al. 2013; de Haan et al. 2016). These field renormalization factors, γ_{field}, are computed using the simulations described in Section 3.4 and are reported in Table 1 on the same reference scale as the analogous factors for the SPT-SZ survey.

The different fields of the SPT-SZ and SPT-ECS surveys have a small amount of overlap at the field boundaries. We correct the field areas such that the total effective survey area corresponds to the unique sky area that is surveyed. These corrections are between 0.03% and 1.9%. SZ detections in the field overlap regions are matched by keeping the candidate with the larger detection significance ξ. Note that this approach is different from the one adopted in de Haan et al. (2016) and Bocquet et al. (2019), who double-counted clusters in the field overlap regions in SPT-SZ in their NC analyses. The exact treatment of the field boundaries has negligible impact on our results; for example, the change in our total predicted cluster counts due to not correcting for the field overlap area is much smaller than the recovered uncertainty.

5.1.2. γ_{ECS} Constraints from the Cluster Abundance

We model the cluster sample as independent Poisson draws from the halo mass function. The likelihood function for the vector of cosmological and scaling relation parameters $\boldsymbol{p}$ is

$$\ln \mathcal{L}(\boldsymbol{p}) = \sum_i \ln \frac{dN(\xi_i, z_i|\boldsymbol{p})}{d\xi dz}$$
$$- \int_{z_{cut}}^{\infty} dz \int_{\xi_{cut}}^{\infty} d\xi \frac{dN(\xi, z|\boldsymbol{p})}{d\xi dz}. \qquad (7)$$

The sum runs over all clusters i in our sample, and

$$\frac{dN(\xi, z|\boldsymbol{p})}{d\xi dz} = \iint dM \, d\zeta \left[P(\xi|\zeta)P(\zeta|M, z, \boldsymbol{p}) \right.$$
$$\left. \frac{dN(M, z|\boldsymbol{p})}{dMdz}\Omega(z, \boldsymbol{p}) \right], \qquad (8)$$

where $\Omega(z, \boldsymbol{p})$ is the survey volume and $dN/dM \, dz$ is the halo mass function given by Tinker et al. (2008). The second line in Equation (7) corresponds to the total number of clusters in the survey.

We analyze the SPT-ECS NC assuming our fixed ΛCDM cosmology. By construction of our scaling relation model, the amplitude A_{SZ} and the correction factor γ_{ECS} (introduced in Section 3.4) are fully degenerate. The constraints on the SZ scaling relation parameters B_{SZ}, C_{SZ}, and the scatter $\sigma_{\ln\zeta}$ from SPT-SZ and SPT-ECS are consistent at the $\ll 1\sigma$ level. To test the consistency of the relative scaling between the two surveys, we analyze the joint NC from SPT-SZ and SPT-ECS. In this analysis, any residual in the relative calibration between the

two surveys is absorbed by γ_{ECS}. We recover

$$\gamma_{ECS} = 1.124 \pm 0.045. \qquad (9)$$

We provide and discuss an alternate calibration of γ_{ECS} in Section 6.1.

5.2. Mass Estimation

The ξ–mass relation defined above in Equations (4)–(6) allows us to compute mass estimates for all sample clusters. We adopt $A_{SZ} = 4.08$, $B_{SZ} = 1.65$, $C_{SZ} = 0.64$, and $\sigma_{\ln\zeta} = 0.20$. These mean scaling relation parameters were determined in Bocquet et al. (2019) for our fixed reference flat ΛCDM cosmology and using the SPT-SZ sample at $\xi > 5$ and $z > 0.25$. As discussed in the previous section, the SZ scaling relation parameters barely shift between an NC analysis using SPT-SZ clusters alone and one using SPT-SZ and SPT-ECS clusters, and we thus use the SPT-SZ-only numbers presented in Bocquet et al. (2019) for consistency with their mass estimates.

5.3. Comparisons to the Planck Cluster Sample

There is naturally significant overlap between the Planck and SPT-ECS cluster samples, as both identify massive clusters by the SZ effect. Here we focus our comparison on the reported masses and redshifts, two quantities critical for cosmological analyses. To directly compare the properties of the two samples for clusters in common, we first associate the catalog from Planck Collaboration et al. (2016b) with the SPT-ECS catalog using a 4′ matching radius and find that 82 SPT candidates (81 confirmed clusters) detected at $\xi > 4$ match Planck systems within this radius.

Overall we find good agreement between the redshifts for matched clusters, with three outliers for which the estimated redshifts reported in the Planck catalog and this work differ by $\delta_z > 0.1$. These three systems each have redshifts in this work from the RM algorithm. Two of the systems (J0046−3911 and J0516−2236) have photometric redshifts reported in the literature, while the third system, J0348−2144 (PSZ2 G215.19−49.65, separated from the SPT position by 0′.58), was associated in the Planck catalog with ACO 3168 (RXC J0347.4−2149), for which a spectroscopic redshift of $z = 0.2399$ was derived from five cluster members in Chon & Böhringer (2012). This system is significantly offset (8′.6, 8′.9) from the SPT and Planck detections, respectively. We instead associate this cluster candidate with a closer (1′.2, 1′.7) and richer ($\lambda = 186$ vs. 10) system at $z = 0.347 \pm 0.008$.

Beyond the direct redshift comparisons, we also provide here redshifts for 13 PSZ2 systems from Planck Collaboration et al. (2016b); 11 of these clusters were not confirmed by the Planck Collaboration. These systems are listed in Table 3. Two of these clusters have previously reported redshifts in Maturi et al. (2019), and a third we associate with ACO S 1048 (Abell et al. 1989). We find good agreement with the Maturi et al. (2019) redshift estimate for PSZ2 G011.92−63.53 but find $\delta_z > 0.2$ for PSZ2 G011.36−72.93.

We can also compare the reported SZ mass estimates for each of these samples. In Figure 7 we show the Planck and SPT clusters in the SPT-ECS and SPT-SZ footprints. In the top panel, plotted as small open symbols, are clusters that are only found in one of the catalogs, while the filled diamonds represent clusters

Table 3
New Confirmations of *Planck* Clusters

PSZ2 Name	z	Separation (arcmin)
PSZ2 G011.36−72.93	0.63 ± 0.04	2.4
PSZ2 G011.92−63.53[a]	0.24 ± 0.02	1.1
PSZ2 G025.07−78.64	0.225 ± 0.033	0.3
PSZ2 G029.55−60.16	0.218	2.8
PSZ2 G210.02−56.38	0.236 ± 0.004	0.7
PSZ2 G216.76−41.84[b]	0.39 ± 0.01	1.1
PSZ2 G221.06−44.05	0.396	0.8
PSZ2 G227.61−84.72	0.432 ± 0.009	0.7
PSZ2 G231.74−70.59	0.275 ± 0.005	1.7
PSZ2 G240.71−74.03	0.40 ± 0.01	0.8
PSZ2 G271.53+36.41	0.51 ± 0.04	0.8
PSZ2 G282.11+38.61	0.30 ± 0.02	1.6
PSZ2 G295.27+32.25	0.71 ± 0.04	1.0

Notes. Redshifts and angular separations (in arcminutes) from SPT cluster positions for PSZ2 Planck Collaboration et al. (2016b) candidates reported without redshifts that are associated with SPT-ECS clusters. We find good agreement with the redshift reported for PSZ2 G011.92−63.53 by Maturi et al. (2019) but find $\delta_z > 0.2$ for PSZ2 G011.36−72.93. We also note that we associate PSZ2 G029.55−60.16 with ACO S 1048 (Abell et al. 1989).
[a] Associated by Planck Collaboration et al. (2016b) with ACO 3296, but no redshift provided.
[b] Associated by Planck Collaboration et al. (2016b) with ACO S 443, but no redshift provided.

that are in both SPT and *Planck*. The 13 *Planck* clusters for which we report a redshift from SPT-ECS in Table 3 are plotted as large open diamonds. Including clusters from the SPT-SZ region brings the joint SPT-*Planck* sample to a total of 150 clusters with mass estimates for which the reported redshifts differ by $\delta_z < 0.1$,[97] and 88 such systems at $z > 0.25$, where SPT masses are expected to be unbiased. In the bottom panel we plot the ratio of SPT to *Planck* mass as a function of redshift and, in the inset, as a function of the SPT mass estimate. Qualitatively, we notice a trend with redshift where at $z < 0.25$ the ratio of the SPT to *Planck* masses is significantly higher than at higher redshifts ($1.44^{+0.05}_{-0.14}$ vs. $1.1^{+0.055}_{-0.03}$). We note that mass estimates for SPT clusters at $z < 0.25$ are more uncertain—though not expected to be biased high—given increased noise contributions from both the primary CMB and atmosphere, as well as the removal of large-scale sky signal by the map filtering.
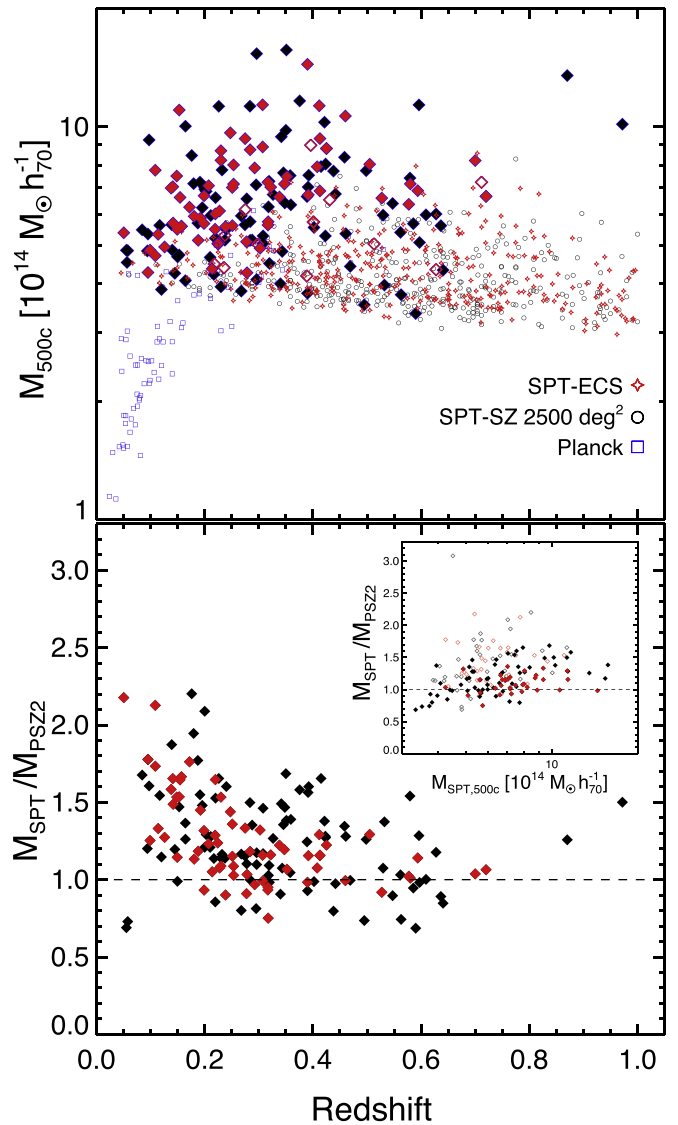
Comparisons to the *Planck* SZ masses are often reported in terms of a mass bias, $1 - b$, where $M_{Planck} = (1 - b)M_{True}$. For purposes of comparison here we treat the SPT masses as the "true" cluster masses and both compute the median mass bias and check for a mass-dependent trend. The latter is achieved via making use of the Bayesian linear regression routines provided by Kelly (2007) and fitting for the power-law index, α:

$$M_{500c\ Planck} \propto M_{500c\ SPT}^{\alpha}. \tag{10}$$

Here we consider only the statistical errors in the SPT and *Planck* masses, as we are directly comparing properties of the same clusters.

As discussed in Battaglia et al. (2016), one must take care in such comparisons, as they can be impacted at the level

Figure 7. Top panel: mass vs. redshift for SPT and *Planck* clusters in the sky area surveyed by SPT. Small open symbols represent clusters that reside only in one of the catalogs, while the filled diamonds represent clusters (plotted at the SPT masses) that are in both SPT-SZ and *Planck* (black, blue outline) and SPT-ECS and *Planck* (red, blue outline). The 13 *Planck* clusters for which we report a redshift in Table 3 are plotted as large open diamonds. In this plot we omit *Planck* clusters that fall within regions excluded by the SPT point-source veto (see Section 3.2) and restrict the x-axis to focus on redshifts where the samples overlap. Bottom panel: again using red diamonds for clusters in common between *Planck* and SPT-ECS and black diamonds for those in *Planck* and SPT-SZ, we plot the ratio of reported SPT to *Planck* masses vs. redshift and (inset) vs. SPT mass. In the inset panel clusters at $z \geqslant 0.25$ ($z < 0.25$) are plotted as filled (open) symbols.

of 3%–15% in $(1 - b)$ by the presence of Eddington bias in the reported *Planck* masses.[98] We follow Battaglia et al. (2016) and recompute the SPT masses not accounting for this bias. Restricting to a subset of 69 clusters where the absolute difference between the *Planck* and SPT S/N was less than 2 (so the bias would be somewhat comparable), we find a median $(1 - b)_{Eddington} = 0.77^{+0.02}_{-0.025}$ and $\alpha = 1.03 \pm 0.14$ for the full sample and $(1 - b)_{Eddington} = 0.80^{+0.09}_{-0.01}$ and $\alpha = 1.3 \pm 0.27$ for 15 such clusters with $0.25 < z < 0.35$ and uncorrected

---

[97] We implement the redshift cut so that the masses would not be significantly different simply from the use of different redshifts in the mass estimation process.

[98] See, e.g., https://wiki.cosmos.esa.int/planckpla2015/index.php/Catalogues#SZ_Catalogue.

$M_{500c \text{ SPT}} > 5.5 \times 10^{14}$ (where both samples are more complete). To aid comparison with previous studies in the literature, we also compute these values for the entire matched sample with *debiased* SPT masses, finding $(1 - b) = 0.83 \pm 0.02$ for the full matched sample and $(1 - b) = 0.91^{+0.01}_{-0.05}$ and $\alpha = 0.75 \pm 0.06$ at $z > 0.25$.

Comparisons between (Eddington-biased) *Planck* and (debiased) SPT mass estimates were previously reported by Planck Collaboration et al. (2016b) and Hilton et al. (2018) for the SPT-SZ and PSZ2 samples. Planck Collaboration et al. (2016b) found the SPT-reported masses to be on average 20% higher than the *Planck* masses—in good agreement with the results derived above with the larger SPT-SZ and SPT-ECS sample. Hilton et al. (2018) explored the relation between SPT-SZ, ACT, and PSZ2 masses, finding the mean mass ratio of ACT to SPT clusters to be 1.00 ± 0.04 for 18 clusters in common between the samples; the SPT-ECS sample provides no additional overlapping systems between ACT and SPT to further this comparison. Hilton et al. (2018) additionally noted a mass-dependent trend between the *Planck* and SPT/ACT masses, finding for the ACT comparison $\alpha = 0.55 \pm 0.18$, a result $\sim 1\sigma$ lower than our value.

A number of studies have also contrasted the estimated *Planck* masses against masses estimated using other observables, with values of $(1 - b)$ ranging from ~ 0.7 to unity (e.g., von der Linden et al. 2014, 0.688 ± 0.072; Hoekstra et al. 2015, 0.76 ± 0.05; Smith et al. 2016, 0.95 ± 0.04; Medezinski et al. 2018, 0.80 ± 0.14). Our recovered values fall within this range. Other works report values for the power-law index, α (e.g., Schellenberger & Reiprich 2017, 0.76 ± 0.08; Mantz et al. 2016, 0.73 ± 0.02), consistent with our measurement when using debiased SPT masses.

We also examine the SPT-ECS footprint for clusters detected by *Planck* but not by SPT. Based on the selection function shown in Figure 6, we expect the SPT-ECS sample to contain essentially all confirmed *Planck* clusters at $z \geqslant 0.25$ in the common sky area. Including the new confirmations discussed above, there are 117 confirmed *Planck* clusters that fall within the SPT-ECS footprint, and 82 of these are associated with SPT cluster candidates at $\xi > 4$. Of the remaining 35 clusters in *Planck* but not confirmed by SPT, 32 are at redshift $z < 0.25$—where the SPT filtering reduces both the completeness of the catalog and the fidelity of the mass estimates—and 5 of these 32 confirmed clusters also excluded because they are in regions excluded by the SPT point-source veto. For the three *Planck* clusters at $z > 0.25$ but not confirmed by SPT, we find that two of these systems match candidates just below the SPT selection threshold, with PSZ2 G244.74$-$28.59 (*Planck* S/N = 5.9, $z = 0.33$) at $\xi = 3.97$ and PSZ2 G251.13$-$78.15 (S/N = 4.6, $z = 0.3$) at $\xi = 3.2$. There is also a radio source nearby to PSZ2 G244.74$-$28.59, which—based on the methodology of Section 3.5—could reduce the ξ value by 0.08–0.7 for a source spectral index of -1 to -0.5. The final unmatched cluster, PSZ2 G282.14+38.29 (S/N = 4.9, $z = 0.33$ with validation from Pan-STARRS), is flagged as having a nearby point source detected at 857 GHz and is measured at $\xi = -0.3$ in our sample. We do not detect a large excess of red sequence galaxies in Pan-STARRS at this cluster location. While the SZ flux from one source (PSZ2 G244.74$-$28.59) may be diminished by the presence of a nearby radio source (which should also influence the *Planck* detection) and we do not independently confirm G282.14+38.29, we find the SPT selection to be consistent with expectations as relates to the PSZ2 sample with 39/42 of the reported *Planck* clusters at $z \geqslant 0.25$ and

not in a point-source vetoed region also in the SPT-ECS sample. Further exploration of the differences between the estimated masses for the *Planck* and SPT samples will require detailed modeling of the selection functions of the two surveys in their jointly accessible mass and redshift ranges and is beyond the scope of this work.

### 5.4. The SPT-ECS Strong-lensing Subsample

The strong gravitational lensing regime, often identified via the presence of highly magnified and multiply imaged background galaxies lensed by foreground gravitational potentials, provides a unique probe of the cores of massive structures. Galaxy clusters have long been recognized as areas in which to productively search for strong gravitational lenses (see review by Meneghetti et al. 2013 and more recent works by Bayliss et al. 2011; Kneib & Natarajan 2011; Diehl et al. 2017; Lotz et al. 2017; Sharon et al. 2019, among many others). We examine the SPT-ECS sample for signatures of strong lensing in the Magellan/PISCO and DES imaging data, as well as in archival and dedicated observations from the *Hubble Space Telescope* (*HST*), the latter from a snapshot program (PID 15307, PI: Gladders) designed to characterize the central regions of massive clusters from SPT-SZ and SPT-ECS.

We find that 44 of the SPT-ECS systems exhibit unambiguous signs of strong lensing; we flag all of these systems in Tables 8 and 9. Some of these systems have been previously identified as strong lenses—see Smail et al. (1991), Sand et al. (2005), Covone et al. (2006), Zitrin et al. (2011), Hamilton-Morris et al. (2012), Gruen et al. (2014), Ebeling et al. (2017, 2018), Newman et al. (2018), Repp & Ebeling (2018), Jacobs et al. (2019), Petrillo et al. (2019), and Coe et al. (2019) —and in the online data for Tables 8 and 9 we also link individual previously known strong lenses to these works. In total over 110 systems from SPT-SZ and SPT-ECS have been identified as strong gravitational lenses; a robust statistical characterization of the PISCO and *HST* data will be the subject of future work. In Figure 8 we display high-quality PISCO data for three of the SPT-ECS strong lenses, as well as data from our *HST* program for the third.

6. The SZ Properties of the Joint SPT-redMaPPer Cluster Sample

Having constructed the SPT-ECS cluster sample, we now leverage the overlap between the DES and SPT surveys to jointly characterize the SZ and richness properties of massive clusters in the Year 3 DES redMaPPer optically selected catalog (see Section 4.1.1). We focus on two properties here: the richness–mass relation of these systems (a key ingredient in cosmological analyses of optical clusters that has been previously probed in numerous works, e.g., Farahi et al. 2016; Geach & Peacock 2017; Simet et al. 2017; Murata et al. 2018; McClintock et al. 2019; Raghunathan et al. 2019), and the offsets between the SZ-based cluster centers and the optical centers as defined by the most probable central galaxy as determined by the RM algorithm. This distribution is useful for both cosmological studies (e.g., as an important input in weak-lensing mass calibration of clusters, Johnston et al. 2007; George et al. 2012; Dietrich et al. 2019) and astrophysical studies, as it probes the dynamical states of clusters (Sanderson et al. 2009; Mann & Ebeling 2012; Rossetti et al. 2016). It can also serve as a test of cluster-centering algorithms.
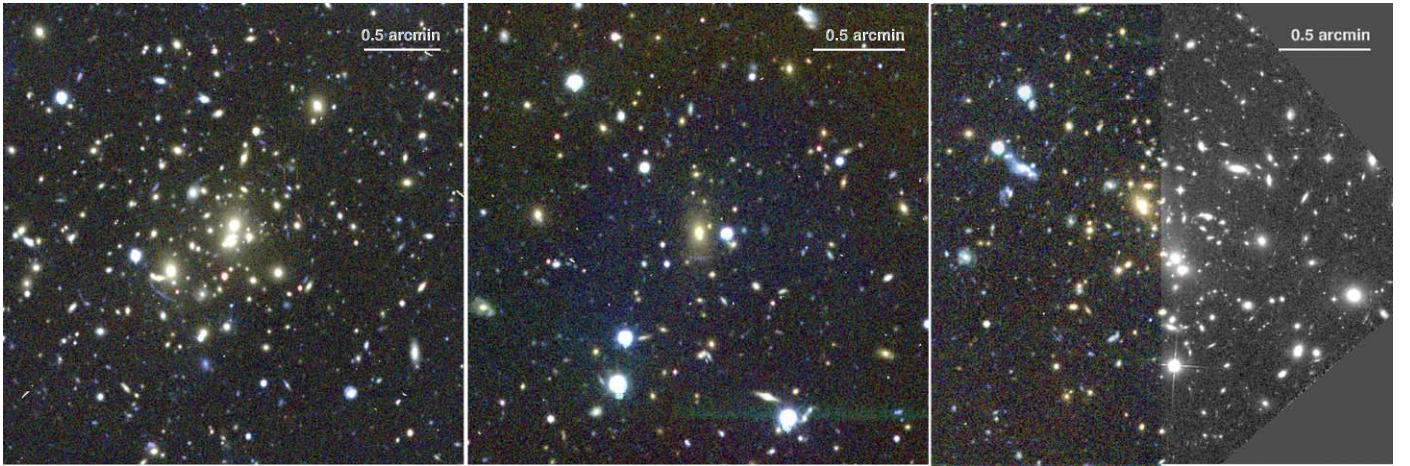
Figure 8. Three strong-lensing clusters from the SPT-ECS survey. Left: SPT-CL J0512−3848 at $z = 0.33$; middle: SPT-CL J1223−3014 at $z = 0.48$; right: SPT-CL J0049−2440 at $z = 0.53$ (first reported as Vidal 14; de Propris et al. 1999). In each panel we show ∼300 s exposure imaging from PISCO in the *gri* bands. These data were taken in good ($<0{\farcs}7$) seeing that enables the strong-lensing identification. In the right panel we also show F110W data from our ongoing *HST* snapshot program.

Following a similar criterion to Saro et al. (2015), we cross-match the optically selected RM sample with SZ clusters by the following:

1. rank-ordering each cluster list: for the SPT clusters by decreasing ξ, and for the RM clusters by decreasing λ;
2. matching each SZ system to the richest RM cluster within $\delta_z = 0.1$ and projected separation between the SZ and RM center <1.5 Mpc at the cluster redshift; and then
3. removing each matched RM cluster from the possible matching pool and continuing the process until the last SZ cluster has been checked for a match.

Note that we do *not* compute a probability of random association here for each SZ cluster in this list, as we have already statistically identified a high-probability association between a cluster detected by the RM algorithm run in "scanning" mode (Section 4.2.1) and the SZ detection. The matching criterion we have chosen in this selection allows us to more fully capture the properties of the RM algorithm when it is run in its standard, blind-search mode; in particular, clusters that scatter low in richness in the blind search are not cut from this analysis. This procedure is also repeated for the full SPT-SZ sample (updating the Saro et al. 2015 results, which centered on the DES Science Verification Region). We confirm 13 new clusters at $\xi > 4.5$ via this method, the majority of which are above the redshift limits reported in B15 (though we found that some of these limits were overestimated in cases of poor seeing). The new clusters are reported in Table 10, and we note that the sample of $\xi < 4.5$ SPT-SZ systems will be discussed in detail in M. Klein et al. (2020, in preparation).

Including SZ cluster candidates detected at $\xi > 4.5$ in the SPT-SZ survey (Bleem et al. 2015b), we find 652 clusters in the ensemble SPT-RM cluster sample. Limiting the redshift range to $z > 0.25$ reduces the sample to 584 systems, and limiting to the volume-limited catalog results in a sample of 249 (410) clusters at $\xi \geqslant 5$ (4); the richness versus ξ (normalized for the field scaling factors; see Section 5.1.1) is shown in Figure 9.

6.1. The Richness–Mass Relation of SPT-RM Clusters

We use the optical richness (λ) measurements of SPT clusters matched to the Y3 RM catalog to calibrate the richness–mass
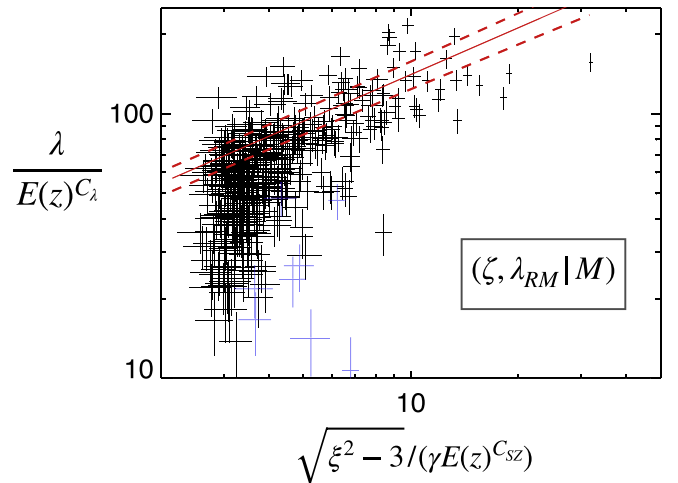
Figure 9. Richness vs. normalized ξ values for the ensemble SPT-RM volume-limited cluster sample; light-blue points are clusters for which $>30\%$ of the DES data was masked in the vicinity of the SPT cluster. The ξ values are normalized by the field scaling factors discussed in Section 5.1.1. Overplotted in red is the best-fit $\lambda - \xi$ relation as calculated in Section 6.1.

relation, taking the SPT selection into account. Assuming our fiducial fixed cosmology, we simultaneously constrain the SZ scaling relation parameters through the NCs of the SPT cluster sample (as discussed in Section 5.1.2) and the parameters of the richness scaling relation. This analysis follows Saro et al. (2015), with the exception that we now also account for the effects of correlated scatter among ζ and richness.

6.1.1. Richness–Mass Relation: Likelihood Function

Along with the ζ–mass relation defined above in Equation (4), we define the richness–mass relation

$$\langle \ln \lambda \rangle = \ln A_\lambda + B_\lambda \ln \left(\frac{M_{500c}}{3 \times 10^{14} \, M_\odot \, h^{-1}} \right)$$

$$+ C_\lambda \ln \left(\frac{E(z)}{E(z = 0.6)} \right). \qquad (11)$$

A covariance matrix describes the correlated intrinsic scatter between the two observables ζ and λ:

$$\Sigma_{\zeta-\lambda} = \begin{pmatrix} \sigma^2_{\ln\zeta} & \rho_{SZ-\lambda}\sigma_{\ln\zeta}\sigma_{\ln\lambda} \\ \rho_{SZ-\lambda}\sigma_{\ln\zeta}\sigma_{\ln\lambda} & \sigma^2_{\ln\lambda} + \lambda^{-1} \end{pmatrix}. \qquad (12)$$

The contribution λ^{-1} to the intrinsic scatter in richness represents the Poisson noise in the number of member galaxies observed at a fixed cluster mass. We note that we expect positive correlation in the scatter between ζ and λ, as both are projected quantities (see, e.g., Angulo et al. 2012).

The joint scaling relation then reads

$$P\left(\begin{bmatrix} \ln\zeta \\ \ln\lambda \end{bmatrix}\middle| M, z\right) = \mathcal{N}\left(\begin{bmatrix} \langle\ln\zeta\rangle(M,z) \\ \langle\ln\lambda\rangle(M,z) \end{bmatrix}, \Sigma_{\zeta-\lambda}\right). \qquad (13)$$

Following Bocquet et al. (2019), the likelihood function for our NCs and richness calibration analysis is

$$\ln\mathcal{L}(\boldsymbol{p}) = \sum_i \ln\frac{dN(\xi_i, z_i|\boldsymbol{p})}{d\xi dz}$$
$$- \int_{z_{cut}}^{\infty} dz \int_{\xi_{cut}}^{\infty} d\xi \frac{dN(\xi, z|\boldsymbol{p})}{d\xi dz}$$
$$+ \sum_j \ln P_j(\text{match}) P(\lambda^{>5}_{obs,j}|\xi_j, z_j, \boldsymbol{p}) \qquad (14)$$

up to a constant, where the first sum runs over all clusters i in the SPT sample above $\xi > 5$ and $z > 0.25$ and the second sum runs over all SPT clusters j for which an RM richness measurement is available. Note that the first two lines represent the NC likelihood defined earlier in Equation (7). The term $P(\text{match}) = 1 - P(\text{random})$ describes the excess probability of matching an RM cluster to an SPT cluster over random associations $P(\text{random})$. The other term in the last line is computed as

$$P(\lambda_{obs}|\xi, z, \boldsymbol{p}) = \iiint dM\, d\zeta\, d\lambda [P(\lambda_{obs}|\lambda)P(\xi|\zeta)$$
$$\times P(\zeta, \lambda|M, z, \boldsymbol{p})P(M|z, \boldsymbol{p})]. \qquad (15)$$

Finally, we account for the richness cut $\lambda_{obs} > 5$ in the volume-limited redMaPPer catalog and evaluate

$$P(\lambda^{>5}_{obs}|\xi, z, \boldsymbol{p}) = \frac{\Theta(\lambda_{obs} > 5)P(\lambda_{obs}|\xi, z, \boldsymbol{p})}{\int_5^{\infty} d\lambda_{obs}\Theta(\lambda_{obs} > 5)P(\lambda_{obs}|\xi, z, \boldsymbol{p})} \qquad (16)$$

with the step function Θ.

6.1.2. Richness–Mass Relation: Results

With this machinery in place we are now ready to explore the mass-richness relation of the SPT-RM sample. Assuming our fiducial cosmology, we evaluate the likelihood presented in Equation (14) of the SPT cluster NCs (which constrains the SZ scaling relation parameters) and the likelihood of the RM richnesses (which constrains the RM richness scaling relation parameters). We only use the SPT-SZ sample for the SPT NCs (to enable an independent constraint on γ_{ECS}, described below), but we use redMaPPer richnesses for the full SPT-SZ+SPT-ECS sample.

We present the constraints on the richness–mass relation in Figure 10 and in Table 4. Compared to previous constraints using 19 clusters from SPT-SZ at $\xi > 4.5$ in the DES Science
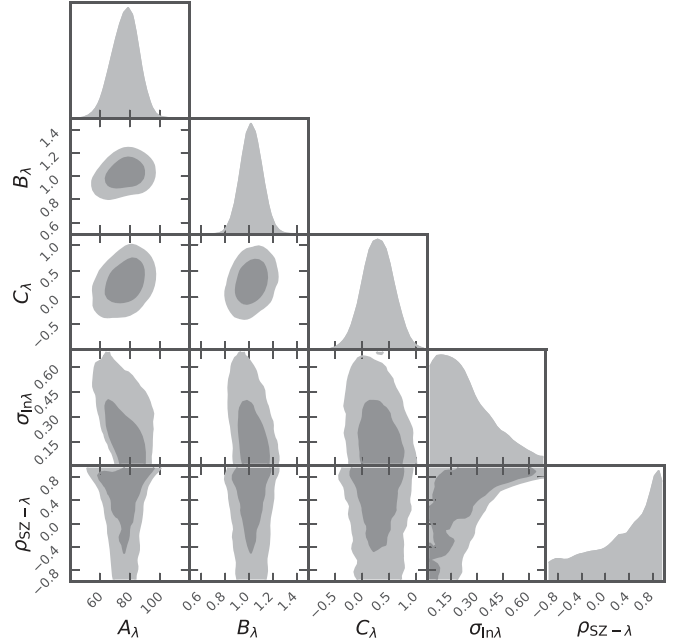
Figure 10. Parameters of the richness–mass relation defined in Equation (11) and the correlation coefficient, $\rho_{SZ-\lambda}$, between the SZ signal (ζ) and richness.

Table 4
Parameters of the Richness–Mass Relation

Parameter	Constraint
A_λ	76.9 ± 8.2
B_λ	1.020 ± 0.080
C_λ	0.29 ± 0.27
$\sigma_{\ln\lambda}$	0.23 ± 0.16
ρ	> -0.78 (95% CL)

Note. The richness–mass relation is defined in Equation (11). We also quote the constraint on the correlation coefficient between the scatter in the SZ signal and richness $\rho_{SZ-\lambda}$. The constraints are obtained using redMaPPer matches to the $\xi > 4.5$, $z > 0.25$ SPT sample.

Verification region (Saro et al. 2015), we find a normalization that is $\sim 1.2\sigma$ higher, with the slope and redshift evolution consistent.

We also compare against the DES weak-lensing analysis of the Year 1 RM sample reported in McClintock et al. (2019), which was also analyzed at our fiducial cosmology. Note that the DES weak-lensing analysis constrains $P(M_{200\,m}|\lambda)$—with masses defined with respect to the *mean* density of the universe—whereas our analysis constrains $P(\lambda|M_{500c})$. We convert M_{500c} to $M_{200\,m}$ assuming a Navarro, Frenk, and White (Navarro et al. 1996) profile and the concentration–mass relation from Child et al. (2018).[99] We invert our relation as

$$P(M_{200\,m}|\lambda) = \int dM_{200\,m} P(\lambda|M_{200\,m}) P(M_{200\,m}) \qquad (17)$$

with the halo mass function prior $P(M_{200\,m})$.

In Figure 11, we show the mass–lambda relation from our work and examples from the literature. At our scaling relation pivot redshift ($z = 0.6$; see Equation (11)), the scaling relation normalizations are consistent at $\lambda \approx 60$ or $M_{200\,m} \approx 5 \times 10^{14} M_\odot$. However, there are some visible differences in the slope. We

---

[99] We use the Colossus package https://bitbucket.org/bdiemer/colossus.
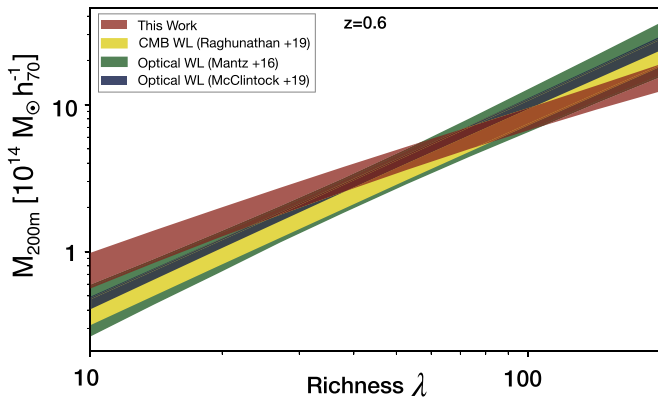
Figure 11. Mass–λ relation evaluated at our pivot redshift $z = 0.6$ determined from SPT cluster NCs assuming our fiducial ΛCDM cosmology. We convert our $\lambda - M_{500c}$ relation to $M_{200\,m} - \lambda$ for ease of comparison with the literature. The relations calibrated from DES Y1 shear or CMB lensing (the latter driven by an informative prior) favor steeper slopes, but there is good agreement at their pivot richness $\lambda_0 = 40$ (McClintock et al. 2019; Raghunathan et al. 2019). The calibration from an X-ray-selected sample with optical weak lensing provides a richness–mass relation that is very similar to the DES Y1 shear result (Mantz et al. 2016).

approximate[100] the slope F_λ in our $P(M_{200\,m}|\lambda)$ relation as

$$F_\lambda \equiv 1/B_\lambda = 0.981 \pm 0.077. \tag{18}$$

We find that our slope is $\sim$30% shallower than the slope from the DES Y1 analysis ($F_\lambda = 1.356 \pm 0.052$; McClintock et al. 2019), with a 4σ offset between the two constraints. To reproduce the slope of the McClintock et al. (2019) relation, we would require a significant shift in our assumed cosmology along the Ω_m and σ_8 degeneracy direction (see, e.g., Costanzi et al. 2019); however, a full cosmological interpretation is beyond the scope of this work and would depend on fully accounting for selection effects in the RM sample under study, as well as on degeneracies and covariances in a wider multidimensional parameter space.

A weak-lensing analysis using data from the Sloan Digital Sky Survey (SDSS) finds an amplitude and slope that are consistent with McClintock et al. (2019) at better than 1σ (Simet et al. 2017). Another weak-lensing study using SDSS data finds a much shallower slope centered at $\lambda \propto M^{0.64}$ using lensing alone; this slope becomes consistent with unity—and thus our measurement—when combining lensing and cluster abundance (Murata et al. 2018). Qualitatively similar results are presented in an analysis of the richness–mass relation using first-year HSC data (Murata et al. 2019). A weak-lensing calibration of an X-ray-selected cluster sample yields constraints on the richness–mass relation that are centered on the results from McClintock et al. (2019), but with large uncertainties (Mantz et al. 2016).

Moving beyond optical weak lensing, two calibrations of the mass–λ relation using lensing of the CMB (Baxter et al. 2018; Raghunathan et al. 2019) recover amplitudes of the mass–λ relation that are compatible with both the calibration from DES Y1 shear measurements and this work. Note, however, that the slope parameters were not constrained by the CMB lensing measurements, where informative priors were applied. The richness–mass relation has also been calibrated using the clustering of clusters (Baxter et al. 2016)

and the measurement of pairwise velocity dispersions (Farahi et al. 2016); both methods show consistency at the 2σ level. Finally, a study of the phase space of galaxy dynamics provides a calibration of the richness–mass relation with a slope that is consistent with unity at $<1\sigma$ (Capasso et al. 2019). However, their relation exhibits strong redshift evolution, which leads to an offset in the relations at our pivot redshift $z = 0.6$.

6.1.3. Richness–Mass Relation: Constraint on γ_{ECS}

By using only the SPT-SZ data in the NCs, we can also use this test to independently evaluate our estimated value for γ_{ECS} presented in Section 5.1.2. We obtain a calibration of the correction factor γ_{ECS} between SPT-SZ and SPT-ECS
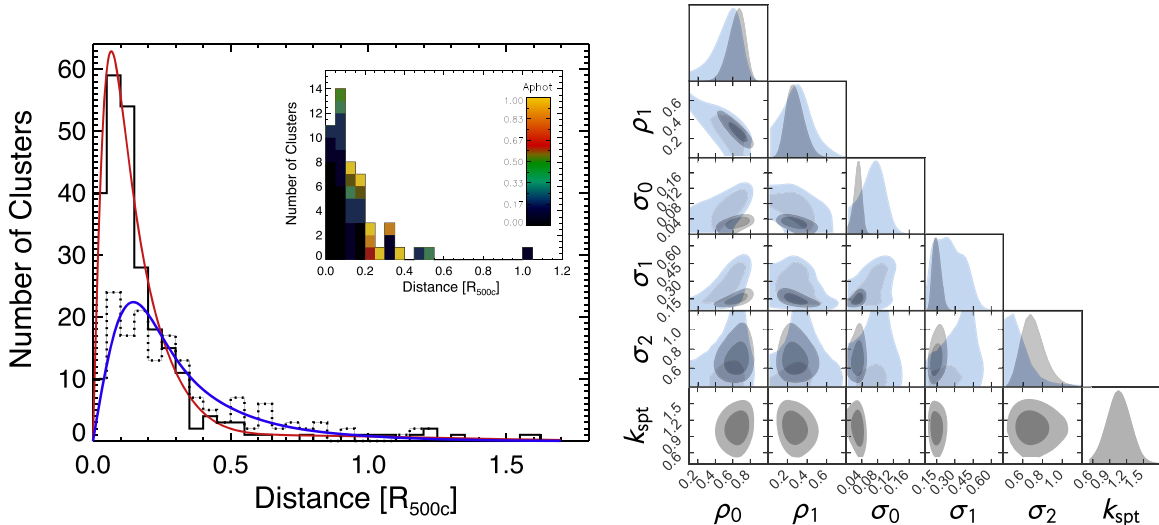
$$\gamma_{ECS} = 1.054 \pm 0.075. \tag{19}$$

This determination of γ_{ECS} is different from the result presented above in Section 5.1.2. In both cases, A_{SZ} is constrained to yield NCs from SPT-SZ that match our fixed fiducial cosmology. In Section 5.1.2, γ_{ECS} was calibrated by also demanding that the SPT-ECS NCs match that cosmology—any relative offset in the amplitude of the ζ–mass relation between SPT-SZ and SPT-ECS is thus absorbed by γ_{ECS}. In the calibration presented here, the redMaPPer richnesses serve as the relative anchor between the SPT-SZ and SPT-ECS surveys. The two determinations of γ_{ECS} agree at the 0.8σ level. We conclude that our empirical modeling of the full SPT-SZ+SPT-ECS sample with an overall amplitude offset is adequate, and when reporting cluster masses we adopt the mean recovered constraint from the more precise NC analysis result as our default.

6.2. redMaPPer-SZ Center Offset Distribution

We next explore the distribution of separations between the redMaPPer- and SPT-determined cluster centers. Based on visual inspection of >100 matched X-ray and RM clusters in SDSS, Rozo & Rykoff (2014) found that the gas centers and central galaxies should be well aligned (within 50 kpc) 80% of the time, with it being rare to find a separation of >300 kpc between the two (results consistent with previous findings by, e.g., Lin & Mohr 2004). In the SDSS sample, the RM algorithm selected the visually identified central galaxy in $86\% \pm 3\%$ of systems and had a long uniform tail to 800 kpc for the remainder of systems. These gas-central galaxy separations were further quantified for RM clusters by Saro et al. (2015) with 19 SPT-RM clusters in DES Science Verification data and Zhang et al. (2019) for 144 (67) systems in SDSS (DES); the latter analysis using archival *Chandra* X-ray data as analyzed in Hollowood et al. (2019). With differing model parameterizations, these works found $\sim$63%–84% of all clusters to be well centered.

Following these previous works, we adopt two different models for this offset distribution for the SPT-RM sample, one modeling offsets relative to the cluster mass scale (via R_{500c}) and the other relative to a cluster extent that scales as a function of RM galaxy richness. Both of these models assume that the offset distribution can be modeled as a central core of well-aligned clusters with small separation combined with a subdominant population of clusters with large offsets. Physically this corresponds to the cluster population being composed

---

[100] Strictly speaking, we compare the slopes of the λ–mass and the mass–λ relations. We checked that the conversion of our relation to mass–λ mostly shifts the amplitude of the relation while leaving the slope almost unchanged.

Figure 12. Left: distribution of offsets between SPT centroids and RM most probable centers as a fraction of R_{500c} for SPT systems in the RM volume-limited sample. The sample at $\xi \geqslant 5$ is plotted in solid black and at $4 < \xi < 5$ with a dotted line. Overplotted in red (blue) is the best fit to the model given by Equation (20) for the high-significance (low-significance) sample. Inset is the offset distribution of the 50 SPT-RM clusters for which the X-ray morphology statistic $A_{\rm phot}$ has been measured. As expected, the more relaxed systems (with smaller $A_{\rm phot}$ values) on average have less spatial separation between the central galaxy and gas center. Right: constraints on the parameters of the offset probability distribution model. Best-fit values are given in Table 5. As the lower-significance sample does not have the power to constrain $\kappa_{\rm SPT}$, we fix its value to the best-fit value from the higher-significance sample for this analysis.

of a mixture of relaxed and merging clusters with some additional scatter introduced via possible misidentification of central galaxies by the RM algorithm.

The dynamical state of the cluster population is also traced by the morphology of the cluster gas, which can be measured by X-ray observations (note that the filtering applied to the SPT maps makes it difficult to extract a robust gas morphological measurement from the SZ data). The X-ray morphology has been measured via the $A_{\rm phot}$ statistic for 50 of the SPT-RM clusters that are also part of a *Chandra* X-ray Visionary Project (XVP; PI: Benson, Nurgaliev et al. 2017); 38 of the systems in the Zhang et al. (2019) DES Y1 analysis mentioned above are part of the SPT-XVP. The $A_{\rm phot}$ statistic is a quantification of the amount of azimuthal asymmetry present in the X-ray photon count distribution and has been shown to be a robust morphological measure even when used on X-ray data with a relatively low number of counts ($\sim$2000 counts per cluster) such as the SPT-XVP observations (Nurgaliev et al. 2013). We plot as an inset in Figure 12 the SZ−optical offset distribution of these 50 clusters. The outlier in this inset plot is SPT-CL J2331−5051 ($A_{\rm phot} = 0.14$), which may be captured pre-merger with SPT-CL J2332 −5053. The RM algorithm has selected what appears to be the central galaxy of the latter cluster and found a smaller structure of $\lambda = 8$ at the location of SPT-CL J2331−5051, which is the more massive system inferred from both the SZ and X-ray observations (see further discussion of this system in Andersson et al. 2011; Huang et al. 2019). The $A_{\rm phot}$ distribution is a continuum, but adopting the somewhat arbitrary choice of McDonald et al. (2017) with $A_{\rm phot} < 0.1$ classified as "relaxed" (17 systems) and $A_{\rm phot} > 0.5$ as "disturbed" (10 systems), we find the median offset of the relaxed (disturbed) systems to be $0.067^{+0.005}_{-0.02} R_{500c}$ ($0.23^{+0.01}_{-0.04} R_{500c}$), with the relaxed systems having a closer alignment between the SZ center and the RM most probable central galaxy, as expected.

### 6.2.1. Offset Distribution Relative to R_{500c}

We first consider the offset distribution relative to the cluster scale R_{500c}. For this analysis we split the cluster population into two parts: a high-significance subset with $\xi \geqslant 5$ (249 clusters, median $\lambda = 81$), which is the threshold used for SPT cosmological analyses (see, e.g., Bocquet et al. 2019), and a lower-significance sample at $4 < \xi < 5$ (161 systems, median $\lambda = 55$). In Figure 12 we plot the distribution of separations between the SZ centroids and RM central galaxies for these two subsamples.

To characterize this distribution, our model follows that of Saro et al. (2015). We have added a third Gaussian term to account for the long tail to large separations. As noted above, such a tail was also previously seen in analyses of SDSS clusters (and given its small sample size, the absence of a significant tail in Saro et al. 2015 is unsurprising). Examination of clusters with the largest separations revealed systems where the RM algorithm identified a bright galaxy near what was the lesser of two SZ peaks in merging clusters (see, e.g., Figure 13 and the discussion of SPT-CL J2331−5051 above), rich systems split into multiple detections (i.e., "mispercolation"; see discussion in Hollowood et al. 2019), systems with significant masking of the optical data near the SPT position, and—for a few of the lower-significance clusters—systems with higher (but still less than 5%) chance of random association between the SZ candidate and RM cluster.

We write the probability distribution as a function of the fractional separation, $x = r_{\rm offset}/R_{500c}$, as

$$P(x) = 2\pi x \left(\frac{\rho_0}{2\pi\sigma_0^2} e^{\frac{-x^2}{2\sigma_0^2}} + \frac{\rho_1}{2\pi\sigma_1^2} e^{\frac{-x^2}{2\sigma_1^2}} + \frac{(1 - \rho_0 - \rho_1)}{2\pi\sigma_2^2} e^{\frac{-x^2}{2\sigma_2^2}} \right)$$

(20)

convolved with the SPT positional uncertainty. The SPT positional uncertainty is given by the cluster detection
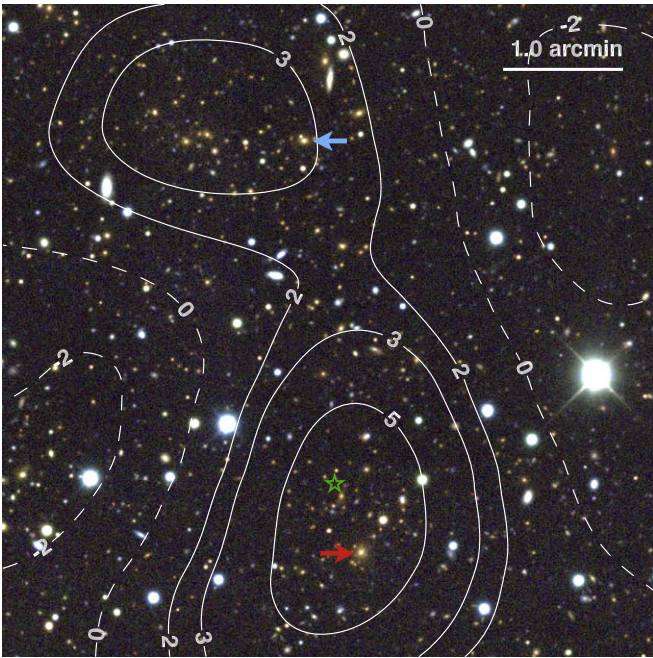
Figure 13. SPT-CL J0543−4250, an illustration of the small fraction of systems where the separation between RM most probable center (identified by the blue arrow, $\lambda = 136$, $z = 0.609 \pm 0.008$) and the SZ center is greater than the RM cluster scale R_λ. The RM algorithm does identify a smaller group at the same redshift (red arrow, $\lambda = 14$), significantly closer to the SPT location (green star). Shown is DES g-, r-, and i-band imaging overlaid with SPT-SZ matched-filter detection contours.

significance, ξ, and detection scale, θ_c,

$$\sigma_{\mathrm{SPT}} = \frac{\sqrt{\theta_{\mathrm{beam}}^2 + (\kappa_{\mathrm{SPT}} \theta_c)^2}}{\xi} \qquad (21)$$

convolved with a general astrometric uncertainty of $4''$–$6''$ (see Section 2.2; W. Everett et al. 2020, in preparation), where $\theta_{\mathrm{beam}} = 1'.3$ is a combination of the $95 + 150\,\mathrm{GHz}$ beams and κ_{SPT} is a parameter of order unity (Story et al. 2011; Song et al. 2012).

We use the emceepackage in Python (Foreman-Mackey et al. 2013) to conduct a Markov Chain Monte Carlo (MCMC) maximum likelihood analysis adopting priors of

$$0 \leqslant \rho \leqslant 1.0$$
$$0 \leqslant \rho_0 - \rho_1 \leqslant 1$$
$$0 \leqslant \sigma_0 \leqslant 0.3$$
$$\sigma_0 < \sigma_1 < 2$$
$$\sigma_1 < \sigma_2 < 3$$
$$0.5 \leqslant \kappa_{\mathrm{SPT}} \leqslant 2.$$

Results for this parameterization for both samples are shown in Figure 12 and reported in Table 5. We note that the lower-significance sample does not have the power to constrain κ_{SPT}, and so we fix it to the best-fit value from the $\xi \geqslant 5$ sample.

For the high-significance, $\xi \geqslant 5$ sample we find that the fraction of clusters in the well-centered component in this version of RM is consistent with Saro et al. (2015) ($\rho_0 = 67^{+6}_{-8}\%$ vs. $63^{+15}_{-25}\%$), with the uncertainty reduced a factor of 2 in this work. The width of this component is slightly smaller ($\sigma_0 = 0.02 \pm 0.01$ vs. 0.07 ± 0.02), and the width of the second component is also smaller ($\sigma_1 = 0.15 \pm 0.03$ vs. 0.25 ± 0.07),

Table 5
Miscentering Model 1 Fits

Parameter	$\xi \geqslant 5$	$4 < \xi < 5$
ρ_0	$0.675^{+0.07}_{-0.08}$	$0.54^{+0.13}_{-0.20}$
σ_0	$0.02^{+0.01}_{-0.01}$	$0.065^{+0.03}_{-0.035}$
ρ_1	$0.25^{+0.08}_{-0.06}$	$0.29^{+0.14}_{-0.16}$
σ_1	$0.15^{+0.03}_{-0.03}$	$0.24^{+0.14}_{-0.11}$
σ_2	$0.70^{+0.125}_{-0.09}$	$0.48^{+0.15}_{-0.07}$
κ_{SPT}	1.0 ± 0.2	$\cdots$

Note. Best-fit miscentering parameters for the SPT-RM volume-limited sample as characterized in Equation (20).

though we note that some of this spread is absorbed in the third Gaussian term that captures the offsets to high R_{500c}.

Turning to the lower-significance sample, we find it overall less well centered than the higher-significance sample, but with the parameters also less well constrained. Future studies using SZ clusters from the 500d SPTpol survey or from SPT-3G will significantly increase the number of lower-mass clusters in our SZ-matched sample and will allow us to more robustly explore miscentering trends as a function of mass.

6.2.2. Offset Distribution Relative to R_λ

As a second model of the SZ–central galaxy offset distribution we explore a miscentering model tied to the RM cluster radius, R_λ, where

$$R_\lambda = \left(\frac{\lambda}{100}\right)^{0.2} h^{-1}\,\mathrm{Mpc}. \qquad (22)$$

R_λ is determined by the RM cluster-finding algorithm and corresponds to the maximum separation between the RM central galaxy and cluster members that contribute to the optical richness measurement. Here we focus on the better-constrained SPT clusters at $\xi > 5$, and we plot this distribution in Figure 14. As can be seen, there are a significant number of systems (14 of 249, 6%) that have offsets greater than R_λ. Examination of these clusters shows, unsurprisingly, that they display similar characteristics to the outliers in the previous subsection (and many are in common). Additionally, it is worth noting that issues that reduce the richness estimate will more adversely affect a fractional offset when the cluster scale is set by the richness measure (e.g., R_λ) as opposed to being set by the SZ mass estimate.

Following McClintock et al. (2019) and Zhang et al. (2019), we model the probability distribution for the separation between SZ centroids and RM central galaxies as the combination of an exponential distribution that reflects the well-centered systems and a Gamma distribution $\Gamma(2, \tau)$ that characterizes those clusters with larger separations:

$$P(x) = \rho \frac{1}{\sigma_\lambda} e^{-\frac{x}{\sigma_\lambda}} + (1 - \rho) \frac{x}{\tau^2} e^{-\frac{x}{\tau}}, \qquad (23)$$

where now $x = r_{\mathrm{offset}}/R_\lambda$, σ_λ characterizes the exponential distribution, τ is the scale parameter of the Gamma distribution function, and, as in the previous model, we also incorporate the SPT positional uncertainties when conducting the fit.

The two-dimensional convolutions required for properly incorporating the SPT positional uncertainty in this model are
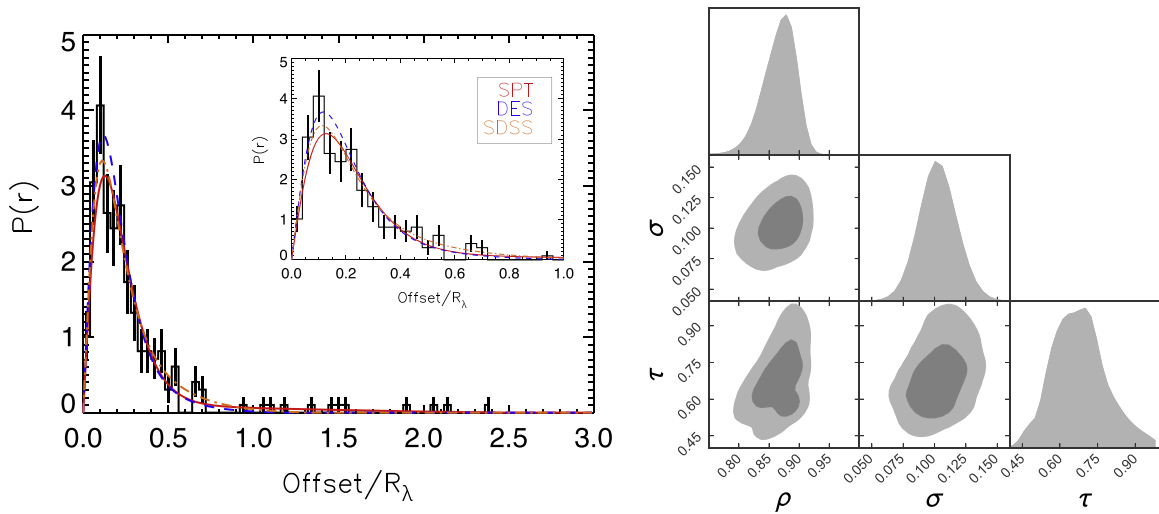
Figure 14. Left: distribution of separations between SPT centers and RM most probable central galaxies as a fraction of the RM cluster radius R_λ for systems at $\lambda > 20$, the richness threshold for DES cosmological analyses. Overplotted in red is the best fit to the SPT data, and in orange (blue) are the best-fit models from Zhang et al. (2019) convolved with the SPT positional uncertainty. The latter analysis characterized the offsets between X-ray peaks and RM central galaxies for 144 (67) systems in SDSS (DES). The large SPT-RM sample shows a higher fraction with large offsets than previous works. Right: best-fit model constraints. These results are overplotted in red in the left panel. We note that the derived value of τ is very sensitive to clusters with large separation.

computationally expensive to repeat many times in an MCMC analysis. Numerical computations of the probability distribution can instead be replaced by relatively inexpensive yet highly precise emulators. For this purpose, we use Gaussian processes (GPs; Rasmussen & Williams 2006), a method that has facilitated robust forward modeling of various astrophysical functions (e.g., Heitmann et al. 2006; Habib et al. 2007 and other applications). We detail the construction and validation of our emulator of the miscentering distribution model in Appendix A.

For this analysis we adopt the priors

$$0.3 \leqslant \rho \leqslant 1.0$$
$$0.001 \leqslant \sigma_\lambda \leqslant 0.25$$
$$0.05 \leqslant \tau \leqslant 1.0.$$

We plot these results in Figure 14 and report the parameter constraints in Table 6. In Figure 14 we also overplot the best-fit model curves from Zhang et al. (2019) convolved with the SPT positional uncertainty.

While Zhang et al. (2019) explored the separation between X-ray peaks and central galaxies, the analysis here quantifies the central galaxy offset from the gas center averaged over a larger scale via the SPT matched filter. This should generally have a small effect; studies with X-ray centering proxies (see, e.g., Mann & Ebeling 2012) have found an additional 20–60 kpc ($\sim 0.02R_\lambda$–$0.06R_\lambda$) scatter in the BCG and X-ray centroid separation (to which our measurement is most analogous) as compared to the X-ray peak to BCG separation, though there can be notable outliers in the case of merging clusters. With this caveat in mind, we find that our results at $\xi > 5$, with $\rho = 0.87^{+0.02}_{-0.03}$ of the clusters within the "well-centered" component of the distribution, agree with previous RM results on DES ($\rho = 0.84^{+0.11}_{-0.07}$) and are higher than those found in SDSS ($\rho = 0.68^{+0.03}_{-0.05}$). However, our recovered value of τ is notably higher than previous results ($\tau = 0.69^{+0.12}_{-0.09}$, vs. $0.16^{+0.11}_{-0.04}$), as it is significantly affected by clusters in the long tail. In comparison, Zhang et al. (2019) only found 1 of 67 systems (1.5%) with gas–BCG separations at $R > R_\lambda$ compared to the 14 (6%) found here. If we reanalyze the cluster sample excluding systems with offsets $R > R_\lambda$, we find ρ and

Table 6
Miscentering Model 2 Fits

Parameter	$\xi \geqslant 5$
ρ	$0.87^{+0.02}_{-0.03}$
σ	$0.12^{+0.015}_{-0.01}$
τ	$0.69^{+0.12}_{-0.09}$

Note. Best-fit miscentering parameters for the SPT-RM volume-limited sample as characterized in Equation (23).

σ_λ significantly less well constrained ($\rho = 0.74^{+0.22}_{-0.30}$, $\sigma_\lambda = 0.105^{+0.045}_{-0.07}$) and τ shifted to lower values consistent with previous work ($\tau = 0.13^{+0.075}_{-0.045}$). It will be important in future weak-lensing analyses to quantify this tail while incorporating all the cluster selection effects relevant to the analysis at hand, as Zhang et al. (2019) found that shifts in τ at the 0.04 level can lead to systematic shifts in the weak-lensing-derived mass calibrations at the level of $\delta \log M_{200} = 0.015$.

7. Conclusions

In this work, we describe the SPT-ECS, a new 2770 deg^2 survey conducted at 95 and 150 GHz using the SPTpol receiver. Using a matched spatial-spectral filter with an SZ detection significance threshold of $\xi \geqslant 5$, we have identified 266 cluster candidates. Of these, we have confirmed and estimated redshifts for 244 clusters using a combination of external optical imaging data, primarily from the DES survey, and targeted observations with the Magellan/PISCO imager. With more incomplete follow-up, we also confirm an additional 204 systems at $4 < \xi < 5$. Approximately two-thirds of the confirmed clusters are first reported in this work.

We estimate cluster masses using a ξ–mass scaling relation, inferred from fitting the observed SZ cluster density at $\xi > 5$ and redshift $z > 0.25$ to a fixed spatially flat ΛCDM cosmology. The SPT-ECS cluster sample has a median redshift of $z = 0.49$ with 20 clusters at $z > 1$, a median mass of $M_{500c} \sim 4.4 \times 10^{14} \, M_\odot \, h^{-1}$, and we unambiguously identify

strong gravitational lensing in 44 systems. Selected data products for this catalog will be hosted at http://pole.uchicago.edu/public/data/sptsz-clusters.

We use 1.4 GHz observations from NVSS to estimate the amount of radio contamination in the SPT-ECS sample. We estimate a median radio contamination of 0.05 in units of the SZ detection significance, which is ∼1% of the SZ signal at the $\xi = 5$ detection threshold. We find that only ∼5% of these candidates would have a predicted radio contamination of >10% compared to the SZ signal level. When extending this test to consider only confirmed clusters at $\xi \gtrsim 4$, we find that <4% of these clusters would have a predicted radio contamination of >10% compared to the SZ signal level. As this test was performed using an SZ-selected sample, it places a lower limit to the radio contamination of the SZ signal of massive clusters, as clusters with extremely bright radio sources could be missed by our SZ selection altogether. However, as discussed in Sections 3.5 and 3.6, such occurrences are expected to be rare at the redshifts of most interest for the SPT sample ($z > 0.25$).

We next associate SZ-selected cluster candidates from a combination of the SPT-ECS and SPT-SZ surveys with clusters from both the *Planck* PSZ2 sample and the DES Year 3 redMaPPer cluster catalog. We find general agreement with previous studies assessing the consistency of *Planck*- and SPT-derived masses and that, as expected, the SPT catalogs contain the majority of PSZ2 clusters at $z > 0.25$ in the SPT footprint.

Considering the SPT and DES RM catalogs, we find 652 clusters that match with a false association probability <5% at $\xi > 4.5$. When restricting this comparison to the redMaPPer volume-limited catalog at $z > 0.25$, we identify 410 systems. Using this sample, we characterize the offset distribution between the SZ center and central galaxy. We find general agreement with the constraints from previous studies (Saro et al. 2015; Zhang et al. 2019) but note that our large sample size allows us to identify a significant tail of clusters to large separations not present in these previous works. We also use the SZ mass estimates to constrain the optical richness–mass relation assuming a fixed standard cosmology. We find that our relation intersects with the previous weak-lensing studies of McClintock et al. (2019) and Raghunathan et al. (2019) at a richness of $\lambda = 60$, but that our SPT-derived relation prefers a 28% shallower slope with the difference significant at the 4.0σ level. To reproduce the slope of the weak-lensing analysis, we would require a significant shift in our assumed cosmology, but we leave any quantitative conclusions to a future analysis. Regardless, our work highlights the value of consistency checks between scaling relations inferred from multiwavelength observations, which should lead to constraints with better-understood systematic uncertainties.

Combined with clusters detected from the SPT-SZ (B15) and SPTpol 100d surveys (Huang et al. 2019), this work increases the number of SZ-detected clusters reported by the SPT to more than 1000. Future SZ-selected cluster catalogs from the SPT will push to higher redshift and lower mass. From SPTpol, this includes the catalog from the completed 500 deg² survey, which is a factor of 5–10 deeper than SPT-ECS (Henning et al. 2018). The ongoing 1500 deg² SPT-3G survey (Benson et al. 2014) is expected to be even deeper, with a mass-selection threshold of $\sim 10^{14}\,M_\odot\,h^{-1}$, which will enable the detection of $\gtrsim 4000$ clusters. This work will complement the wide-area cluster surveys to be conducted at X-ray (*eROSITA*; Predehl et al. 2010; Merloni et al. 2012) and optical/IR wavelengths

(e.g., LSST, LSST Science Collaboration et al. 2009; *Euclid*, Euclid Collaboration et al. 2019; *WFIRST*, Spergel et al. 2015), as well as SZ surveys by AdvACT (Henderson et al. 2016) and Simons Observatory (Simons Observatory Collaboration et al. 2019), with all of the SZ surveys ultimately setting the stage for the next-generation CMB-S4 survey (Abazajian et al. 2016; CMB-S4 Collaboration et al. 2019).

Appendix A
Offset Distribution Emulator Construction

In this section we describe the construction of our emulator of the SZ–RM central galaxy offset distribution discussed in Section 6.2.2. This distribution is modeled as the SPT positional uncertainty (see Equation (21)) convolved with

$$P(x) = \rho \frac{1}{\sigma_\lambda} e^{-\frac{x}{\sigma_\lambda}} + (1 - \rho) \frac{x}{\tau^2} e^{-\frac{x}{\tau}}, \qquad (24)$$

where $x = r_{\mathrm{offset}}/R_\lambda$, σ_λ characterizes the exponential distribution, and τ is the scale parameter of the Gamma distribution function. The training probability distributions $p(x, \theta)$ are generated at $N = 1024$ points on a Latin hypercube sampling (LHS) design of the three centering model parameters, as well as the SPT positional uncertainty scaled by the RM size (converted to radians) $\theta = \{\rho, \sigma_\lambda, \tau, \sigma_{\mathrm{SPT}}/\theta_\lambda\}$. As shown in Cosmic Emulators (Heitmann et al. 2016), the space-filling properties of LHS are well suited for GP interpolation on a relatively small number of training points. The range of our centering model parameters is identical to the flat priors in our likelihood analysis and the SPT positional uncertainty trained over the range $0.0 \leqslant \sigma_{\mathrm{SPT}}/\theta_\lambda \leqslant 1.0$.

Our emulation strategy also follows that of the Cosmic Emulators. That is, we first perform a singular value decomposition of probability $p(x, \theta)$ values in 100 bins (spanning separations from 0 to R_λ). Weights of 16 truncated orthogonal bases are then modeled as independent functions of input parameters $\{\rho, \sigma_\lambda, \tau, \sigma_{\mathrm{SPT}}/R_\lambda\}$ using GP as a local interpolating scheme. The key ingredient of *learning* in GP modeling is the configuration of the covariance function and determination of the associated hyperparameters, which we find using Bayesian optimization. We also check the robustness of the emulator accuracy with different choices of covariance functions.

The fully trained emulator is validated on the parameter values within the limits of the Latin hypercube, but not at the specific points where the emulator is fitted. The evaluation time for the trained emulator is less than 0.001 s per computation, delivering a speed-up of 1000 over numerical calculation of $p(x, \theta)$. This is crucial for quick explorations of the posterior distribution of parameters, where our GP emulator is implemented in the MCMC likelihood calculation.

Appendix B
Associations with LRGs from the 2dFLenS Survey

SPT clusters, redshift estimates, and associated LRG spectroscopic redshifts for clusters associated with LRGs in the 2dFLenS Survey (see Section 4.2.3) are provided in Table 7. SPT-CL J0302−3306 and SPT-CL J0319−2853 were targeted in a spare-fiber program. The full 2dFLenS redshift catalog is available at http://2dflens.swin.edu.au/.

Table 7
Associations with 2dFLenS LRGs

SPT ID	z	2dFLenS z(s)	Offset (arcmin)
SPT-CL J0000−2805	0.23 ± 0.03	0.283	0.64
SPT-CL J0014−3022	0.307	0.308, 0.317	1.04, 1.68
SPT-CL J0036−3144	0.41 ± 0.01	0.413	0.18
SPT-CL J0042−2831	0.109	0.110, 0.109	1.16, 2.46
SPT-CL J0100−3246	0.53 ± 0.01	0.532	1.76
SPT-CL J0114−2820	0.43 ± 0.01	0.441, 0.447	1.03, 1.22
SPT-CL J0115−2917	0.41 ± 0.01	0.397	1.27
SPT-CL J0121−3355	0.57 ± 0.01	0.579	1.28
SPT-CL J0152−2853	0.413	0.416, 0.406	0.25, 0.85
SPT-CL J0158−2910	0.57 ± 0.01	0.576	2.11
SPT-CL J0159−3010	0.69 ± 0.01	0.699, 0.703	1.21, 1.57
SPT-CL J0159−3331	0.40 ± 0.01	0.411, 0.406	0.42, 2.31
SPT-CL J0202−2812	0.12 ± 0.01	0.111	2.32
SPT-CL J0202−3027	0.48 ± 0.01	0.489, 0.493	0.27, 1.52
SPT-CL J0206−2921	0.28 ± 0.01	0.273	1.60
SPT-CL J0215−2948	0.25 ± 0.01	0.256	2.36
SPT-CL J0217−3200	0.35 ± 0.01	0.341	0.26
SPT-CL J0218−3142	0.27 ± 0.01	0.275, 0.269, 0.267	0.19, 0.74, 1.68
SPT-CL J0224−3223	0.54 ± 0.01	0.545, 0.545	1.36, 1.86
SPT-CL J0241−2839	0.238	0.226, 0.237	0.89, 2.45
SPT-CL J0242−3123	0.50 ± 0.01	0.491	1.01
SPT-CL J0302−3209	0.32 ± 0.01	0.327, 0.325	0.18, 1.67
SPT-CL J0302−3306	0.73 ± 0.01	0.752	0.66
SPT-CL J0303−2736	0.27 ± 0.01	0.261	0.73
SPT-CL J0305−3229	0.53 ± 0.01	0.529	0.33
SPT-CL J0307−2840	0.253	0.250	0.45
SPT-CL J0309−3209	0.54 ± 0.01	0.526	2.35
SPT-CL J0319−2853	0.36 ± 0.01	0.355	0.04
SPT-CL J0319−3345	0.41 ± 0.01	0.411	0.46
SPT-CL J2159−2846	0.43 ± 0.04	0.423, 0.431	0.89, 2.19
SPT-CL J2220−3509	0.154	0.152	1.55
SPT-CL J2234−3033	0.251	0.246	0.73
SPT-CL J2234−3159	0.57 ± 0.04	0.557	0.46
SPT-CL J2251−3324	0.24 ± 0.02	0.230, 0.231	0.43, 1.00
SPT-CL J2253−3344	0.224	0.228	0.07
SPT-CL J2258−3447	0.317	0.307, 0.308	0.64, 0.97
SPT-CL J2321−2725	0.67 ± 0.04	0.658	0.92
SPT-CL J2335−3256	0.51 ± 0.04	0.490, 0.511	1.91, 2.16
SPT-CL J2336−3205	0.63 ± 0.04	0.619, 0.613, 0.623	0.27, 1.52, 2.43

Note. For each cluster we report the cluster name, spectroscopic (three digits) or photometric (two digits with uncertainty) redshift, the spectroscopic redshifts of the 2dFLenS LRGS, and the spatial separation of these LRGs from the SPT cluster location.

(This table is available in machine-readable form.)

Appendix C
The Cluster Catalogs

In this appendix we provide three different tables: the complete cluster candidate list at $\xi > 5$ from SPT-ECS (Table 8), the confirmed sample from SPT-ECS at $4 < \xi < 5$ (Table 9), and, finally, newly confirmed clusters at $\xi > 4.5$ from the 2500d SPT-SZ survey (Table 10; Bleem et al. 2015b).

The SPT-SZ clusters were confirmed using our RM association process described in Section 4.2.1. The data from these tables, including references for the sources of spectroscopic redshifts, photometric redshifts (when taken from the literature), and strong-lensing information (where previously known), as well as additional notes on individual clusters, are available online at http://pole.uchicago.edu/public/data/sptsz-clusters.

Table 8
Galaxy Cluster Candidates above $\xi = 5$ in the SPTpol Extended Cluster Survey

SPT ID	R.A. (J2000)	Decl. (J2000)	Best		Redshift	M_{500c} $(10^{14}h_{70}^{-1}\,M_\odot)$	λ	Image Source	Notes
			ξ	θ_c					
SPT-CL J0000−2518	0.0723	−25.3039	5.07	1.50	⋯	⋯	⋯	1	⋯
SPT-CL J0005−3751	1.4383	−37.8544	6.34	0.75	0.483 ± 0.007	$5.42^{+0.89}_{-0.89}$	86 ± 5	3	SL
SPT-CL J0005−3443	1.4877	−34.7193	5.51	2.00	0.114	$5.32^{+0.90}_{-1.00}$	105 ± 5	8	⋯
SPT-CL J0012−3537	3.0433	−35.6226	5.26	2.25	0.69 ± 0.02	$4.38^{+0.80}_{-0.89}$	73 ± 5	3	⋯
SPT-CL J0012−3346	3.1112	−33.7782	6.70	1.00	0.68 ± 0.01	$5.37^{+0.82}_{-0.85}$	101 ± 6	3	⋯
SPT-CL J0014−3022	3.5727	−30.3831	18.29	1.50	0.307	$11.39^{+1.15}_{-1.38}$	⋯	8	SL
SPT-CL J0014−2024	3.6932	−20.4087	5.64	1.00	0.317	$5.62^{+0.98}_{-0.98}$	⋯	8	⋯
SPT-CL J0020−2543	5.1731	−25.7276	7.14	1.50	0.141	$7.04^{+0.97}_{-1.08}$	101 ± 18	8	⋯
SPT-CL J0028−2649	7.0111	−26.8205	7.03	0.50	0.75 ± 0.01	$5.93^{+0.84}_{-0.95}$	77 ± 5	3	⋯
SPT-CL J0035−2015	8.8608	−20.2635	8.40	1.25	0.352	$7.48^{+0.95}_{-1.08}$	⋯	8	⋯

Note. Here we report for each cluster candidate detected at $\xi > 5$ the candidate name, position, detection significance (ξ), the β-model core radius (in arcminutes) corresponding to this significance (see Section 3), and the source of follow-up imaging. When a candidate is confirmed as a cluster, we also report its redshift and mass, richness from RM in "scanning mode" (where available; see Section 4.2.1), and flag if the system has been identified as a strong gravitational lens (SL) or if the estimated radio contamination to the SZ signal exceeds 10% (RC; see Section 3.5). The key for the Image Source column is as follows: [1] Pan-STARRS, [2] Magellan/PISCO, [3] DES, [4] Magellan/FourStar, [5] *Spitzer*/IRAC, [6] *WISE*, [7] literature photometric redshift, [8] spectroscopic redshift. Generally, data from Pan-STARRS are deep enough to confirm clusters to $z \sim 0.6$, DES and PISCO to $z \sim 0.8$–1.0, FourStar to $z \sim 1.2$, and *Spitzer* to $z \sim 1.5$.

(This table is available in its entirety in machine-readable form.)

Table 9
Confirmed Galaxy Clusters $4 < \xi < 5$ in the SPTpol Extended Cluster Survey

SPT ID	R.A. (J2000)	Decl. (J2000)	Best		Redshift	M_{500c} $(10^{14}h_{70}^{-1}\,M_\odot)$	λ	Imaging	Notes
			ξ	θ_c					
SPT-CL J0000−3838	0.0118	−38.6467	4.37	2.25	0.305 ± 0.007	$4.25^{+0.71}_{-0.95}$	49 ± 3	3	⋯
SPT-CL J0000−2805	0.0906	−28.0947	4.79	2.50	0.23 ± 0.03	$5.05^{+0.91}_{-1.09}$	⋯	1	⋯
SPT-CL J0001−3446	0.3080	−34.7729	4.23	0.25	0.73 ± 0.02	$3.72^{+0.57}_{-0.83}$	45 ± 7	3	⋯
SPT-CL J0011−2841	2.8272	−28.6859	4.13	0.25	0.089 ± 0.006	$4.79^{+0.74}_{-1.05}$	22 ± 5	3	⋯
SPT-CL J0019−2026	4.7834	−20.4475	4.95	1.25	0.277	$5.12^{+0.98}_{-1.05}$	⋯	8	⋯
SPT-CL J0020−2634	5.2048	−26.5799	4.14	0.25	0.233 ± 0.006	$4.62^{+0.74}_{-1.02}$	22 ± 4	3	⋯
SPT-CL J0023−3252	5.7941	−32.8672	4.28	0.75	0.66 ± 0.01	$3.83^{+0.61}_{-0.84}$	45 ± 4	3	⋯
SPT-CL J0025−3618	6.3664	−36.3085	4.53	0.25	0.215 ± 0.005	$4.48^{+0.77}_{-0.99}$	21 ± 2	3	⋯
SPT-CL J0027−3729	6.9845	−37.4854	4.32	0.25	0.83 ± 0.02	$3.66^{+0.56}_{-0.81}$	23 ± 4	3	⋯
SPT-CL J0033−3413	8.4038	−34.2293	4.52	0.25	0.233 ± 0.005	$4.46^{+0.77}_{-0.97}$	33 ± 3	3	⋯
SPT-CL J0036−2104	9.1838	−21.0828	4.23	0.25	0.356 ± 0.009	$4.52^{+0.74}_{-1.00}$	72 ± 7	3	⋯
SPT-CL J0036−3144	9.2171	−31.7460	4.49	1.75	0.41 ± 0.01	$4.23^{+0.73}_{-0.94}$	72 ± 4	3	RC

Note. Same as Table 8, but now for confirmed candidates at $4 < \xi < 5$.

(This table is available in its entirety in machine-readable form.)

Table 10
Newly Confirmed Galaxy Clusters at $\xi > 4.5$ in the SPT-SZ Survey

SPT ID	R.A. (J2000)	Decl. (J2000)	Best		Redshift	M_{500c} $(10^{14} h_{70}^{-1} M_\odot)$	λ
			ξ	θ_c			
SPT-CL J2352−5846	358.0510	−58.7758	5.18	0.75	0.167 ± 0.006	$3.86^{+0.67}_{-0.77}$	23 ± 6
SPT-CL J0013−5714	3.3029	−57.2373	5.11	1.50	0.63 ± 0.01	$3.70^{+0.67}_{-0.76}$	29 ± 3
SPT-CL J2328−4616	352.0576	−46.2802	4.84	2.75	0.224 ± 0.005	$3.94^{+0.70}_{-0.84}$	25 ± 3
SPT-CL J0048−4450	12.1743	−44.8475	4.82	0.50	0.595 ± 0.009	$3.55^{+0.61}_{-0.77}$	55 ± 5
SPT-CL J2339−4058	354.7996	−40.9697	4.75	0.25	0.60 ± 0.01	$3.50^{+0.61}_{-0.76}$	31 ± 3
SPT-CL J2136−5723	324.1203	−57.3968	4.72	1.00	0.284 ± 0.007	$3.65^{+0.63}_{-0.78}$	42 ± 3
SPT-CL J2158−4851	329.5692	−48.8533	4.64	0.25	0.490 ± 0.008	$3.69^{+0.65}_{-0.82}$	58 ± 6
SPT-CL J0501−4455	75.2932	−44.9270	4.59	0.25	0.433 ± 0.010	$3.80^{+0.65}_{-0.85}$	80 ± 5
SPT-CL J0353−5312	58.3058	−53.2095	4.54	0.25	0.65 ± 0.01	$3.24^{+0.54}_{-0.70}$	31 ± 3
SPT-CL J0323−4913	50.9166	−49.2215	4.54	0.50	0.37 ± 0.01	$3.51^{+0.59}_{-0.77}$	29 ± 3
SPT-CL J0437−5307	69.2599	−53.1206	4.52	0.25	0.301 ± 0.007	$3.54^{+0.60}_{-0.79}$	38 ± 3
SPT-CL J0500−4551	75.2108	−45.8564	4.51	0.75	0.242 ± 0.005	$3.96^{+0.68}_{-0.88}$	38 ± 4
SPT-CL J0250−4714	42.6656	−47.2385	4.50	1.25	0.475 ± 0.008	$3.50^{+0.57}_{-0.77}$	39 ± 3

Note. SPT-SZ clusters newly confirmed using the RM algorithm in "scanning mode"; see Section 4.2.1. When overlapping, column entries match Table 8.

(This table is available in machine-readable form.)

ORCID iDs

L. E. Bleem https://orcid.org/0000-0001-7665-5079
S. Bocquet https://orcid.org/0000-0002-4900-805X
B. Stalder https://orcid.org/0000-0003-0973-4900
P. A. R. Ade https://orcid.org/0000-0002-5127-0401
J. Annis https://orcid.org/0000-0002-0609-3987
M. L. N. Ashby https://orcid.org/0000-0002-3993-0745
B. A. Benson https://orcid.org/0000-0002-5108-6823
F. Bianchini https://orcid.org/0000-0003-4847-3483
M. Brodwin https://orcid.org/0000-0002-4208-798X
E. Buckley-Geer https://orcid.org/0000-0002-3304-0733
A. Carnero Rosell https://orcid.org/0000-0003-3044-5150
M. Carrasco Kind https://orcid.org/0000-0002-4802-3194
J. Carretero https://orcid.org/0000-0002-3130-0204
T. M. Crawford https://orcid.org/0000-0001-9000-5013
J. De Vicente https://orcid.org/0000-0001-8318-6813
S. Desai https://orcid.org/0000-0002-0466-3288
H. T. Diehl https://orcid.org/0000-0002-8357-7467
J. P. Dietrich https://orcid.org/0000-0002-8134-9591
T. F. Eifler https://orcid.org/0000-0002-1894-3301
J. Frieman https://orcid.org/0000-0003-4079-3263
J. García-Bellido https://orcid.org/0000-0002-9370-8360
D. W. Gerdes https://orcid.org/0000-0001-6942-2736
D. Gruen https://orcid.org/0000-0003-3270-7644
R. A. Gruendl https://orcid.org/0000-0002-4588-6517
G. Gutierrez https://orcid.org/0000-0003-0825-0517
D. L. Hollowood https://orcid.org/0000-0002-9369-4157
G. Khullar https://orcid.org/0000-0002-3475-7648
N. Kuropatkin https://orcid.org/0000-0003-2511-0946
C. Lidman https://orcid.org/0000-0003-1731-0497
G. Mahler https://orcid.org/0000-0003-3266-2001
J. L. Marshall https://orcid.org/0000-0003-0710-9474
P. Melchior https://orcid.org/0000-0002-8873-5065
F. Menanteau https://orcid.org/0000-0002-1372-2534
R. Miquel https://orcid.org/0000-0002-6610-4836
A. Palmese https://orcid.org/0000-0002-6011-0530
D. Parkinson https://orcid.org/0000-0002-7464-2351
F. Paz-Chinchón https://orcid.org/0000-0003-1339-2683
A. A. Plazas https://orcid.org/0000-0002-2598-0514
C. L. Reichardt https://orcid.org/0000-0003-2226-9169

J. D. Remolina González https://orcid.org/0000-0002-7868-9827
A. K. Romer https://orcid.org/0000-0002-9328-879X
A. Roodman https://orcid.org/0000-0001-5326-3486
E. S. Rykoff https://orcid.org/0000-0001-9376-3135
E. Sanchez https://orcid.org/0000-0002-9646-8198
K. Sharon https://orcid.org/0000-0002-7559-0864
M. Smith https://orcid.org/0000-0002-3321-1432
M. Soares-Santos https://orcid.org/0000-0001-6082-8529
A. A. Stark https://orcid.org/0000-0002-2718-9996
E. Suchyta https://orcid.org/0000-0002-7047-9358
G. Tarle https://orcid.org/0000-0003-1704-0781
J. Weller https://orcid.org/0000-0002-8282-2010
N. Whitehorn https://orcid.org/0000-0002-3157-0407
W. L. K. Wu https://orcid.org/0000-0001-5411-6920

References

Abazajian, K. N., Adshead, P., Ahmed, Z., et al. 2016, arXiv:1610.02743
Abbott, T. M. C., Abdalla, F. B., Allam, S., et al. 2018, ApJS, 239, 18
Abell, G. O. 1958, ApJS, 3, 211
Abell, G. O., Corwin, H. G., Jr., & Olowin, R. P. 1989, ApJS, 70, 1
Adami, C., Giles, P., Koulouridis, E., et al. 2018, A&A, 620, A5
Alberts, S., Pope, A., Brodwin, M., et al. 2016, ApJ, 825, 72
Allen, S. W., Evrard, A. E., & Mantz, A. B. 2011, ARA&A, 49, 409
Andersson, K., Benson, B. A., Ade, P. A. R., et al. 2011, ApJ, 738, 48
Angulo, R. E., Springel, V., White, S. D. M., et al. 2012, MNRAS, 426, 2046
Ashby, M. L. N., Stern, D., Brodwin, M., et al. 2009, ApJ, 701, 428
Austermann, J. E., Aird, K. A., Beall, J. A., et al. 2012, Proc. SPIE, 8452, 84521E
Bai, L., Marcillac, D., Rieke, G. H., et al. 2007, ApJ, 664, 181
Barrena, R., Streblyanska, A., Ferragamo, A., et al. 2018, A&A, 616, 42
Battaglia, N., Bond, J. R., Pfrommer, C., & Sievers, J. L. 2012, ApJ, 758, 75
Battaglia, N., Leauthaud, A., Miyatake, H., et al. 2016, JCAP, 2016, 013
Baxter, E., Clampitt, J., Giannantonio, T., et al. 2016, MNRAS, 461, 4099
Baxter, E. J., Raghunathan, S., Crawford, T. M., et al. 2018, MNRAS, 476, 2674
Bayliss, M. B., Hennawi, J. F., Gladders, M. D., et al. 2011, ApJS, 193, 8
Bender, A. N., Kennedy, J., Ade, P. A. R., et al. 2016, MNRAS, 460, 3432
Benson, B. A., Ade, P. A. R., Ahmed, Z., et al. 2014, Proc. SPIE, 9153, 1
Bertin, E., & Arnouts, S. 1996, A&AS, 117, 393
Bertin, E., Mellier, Y., Radovich, M., et al. 2002, ASP Conf. Ser. 281, Astronomical Data Analysis Software and Systems XI, ed. D. A. Bohlender, D. Durand, & T. H. Handley (San Francisco, CA: ASP), 228

Biesiadzinski, T., McMahon, J. J., Miller, C. J., Nord, B., & Shaw, L. 2012, ApJ, 757, 1

Blake, C., Amon, A., Childress, M., et al. 2016, MNRAS, 462, 4240

Bleem, L. E., Stalder, B., Brodwin, M., et al. 2015a, ApJS, 216, 20

Bleem, L. E., Stalder, B., de Haan, T., et al. 2015b, ApJS, 216, 27

Bocquet, S., Dietrich, J. P., Schrabback, T., et al. 2019, ApJ, 878, 55

Böhringer, H., Schuecker, P., Guzzo, L., et al. 2004, A&A, 425, 367

Brodwin, M., Stanford, S. A., Gonzalez, A. H., et al. 2013, ApJ, 779, 138

Bruzual, G., & Charlot, S. 2003, MNRAS, 344, 1000

Burenin, R. A., Bikmaev, I. F., Khamitov, I. M., et al. 2018, AstL, 44, 297

Burgess, A. M., & Hunstead, R. W. 2006, AJ, 131, 114

Calabretta, M. R., & Greisen, E. W. 2002, A&A, 395, 1077

Capasso, R., Mohr, J. J., Saro, A., et al. 2019, MNRAS, 486, 1594

Carlstrom, J. E., Ade, P. A. R., Aird, K. A., et al. 2011, PASP, 123, 568

Carlstrom, J. E., Holder, G. P., & Reese, E. D. 2002, ARA&A, 40, 643

Cavagnolo, K., Donahue, M., Voit, G., & Sun, M. 2008, ApJ, 682, 821

Cavaliere, A., & Fusco-Femiano, R. 1976, A&A, 49, 137

Chambers, K. C., Magnier, E. A., Metcalfe, N., et al. 2016, arXiv:1612.05560

Child, H. L., Habib, S., Heitmann, K., et al. 2018, ApJ, 859, 55

Chluba, J., Nagai, D., Sazonov, S., & Nelson, K. 2012, MNRAS, 426, 510

Chon, G., & Böhringer, H. 2012, A&A, 538, A35

CMB-S4 Collaboration, Abazajian, K., Addison, G., et al. 2019, arXiv:1907.04473

Coble, K., Ade, P. A. R., Bock, J. J., et al. 2003, arXiv:astro-ph/0301599

Coe, D., Salmon, B., Bradac, M., et al. 2019, ApJ, 884, 85

Condon, J. J., Cotton, W. D., Greisen, E. W., et al. 1998, AJ, 115, 1693

Costanzi, M., Rozo, E., Simet, M., et al. 2019, MNRAS, 488, 4779

Covone, G., Kneib, J.-P., Soucail, G., et al. 2006, A&A, 456, 409

Crites, A. T., Henning, J. W., Ade, P. A. R., et al. 2015, ApJ, 805, 36

Czakon, N. G., Sayers, J., Mantz, A., et al. 2015, ApJ, 806, 18

Dalton, G. B., Maddox, S. J., Sutherland, W. J., & Efstathiou, G. 1997, MNRAS, 289, 263

Dark Energy Survey Collaboration, Abbott, T. M. C., Abdalla, F. B., et al. 2018, ApJS, 239, 18

De Bernardis, F., Stevens, J. R., Hasselfield, M., et al. 2016, Proc. SPIE, 9910, 991014

de Haan, T., Benson, B. A., Bleem, L. E., et al. 2016, ApJ, 832, 95

de Jong, J. T. A., Verdoes Kleijn, G. A., Kuijken, K. H., & Valentijn, E. A. 2013, ExA, 35, 25

de Propris, R., Stanford, S. A., Eisenhardt, P. R., Dickinson, M., & Elston, R. 1999, AJ, 118, 719

De Zotti, G., Ricci, R., Mesa, D., et al. 2005, A&A, 431, 893

Diehl, H. T., Buckley-Geer, E. J., Lindgren, K. A., et al. 2017, ApJS, 232, 15

Dietrich, J. P., Bocquet, S., Schrabback, T., et al. 2019, MNRAS, 483, 2871

Dreyer, J. L. E. 1888, MmRAS, 49, 1

Eales, S., Dunne, L., Clements, D., et al. 2010, PASP, 122, 499

Ebeling, H., Edge, A. C., Mantz, A., et al. 2010, MNRAS, 407, 83

Ebeling, H., Qi, J., & Richard, J. 2017, MNRAS, 471, 3305

Ebeling, H., Stockmann, M., Richard, J., et al. 2018, ApJL, 852, L7

Edge, A., Sutherland, W., Kuijken, K., et al. 2013, Msngr, 154, 32

Eisenhardt, P. R. M., Brodwin, M., Gonzalez, A. H., et al. 2008, ApJ, 684, 905

Erler, J., Basu, K., Chluba, J., & Bertoldi, F. 2018, MNRAS, 476, 3360

Euclid Collaboration, Adam, R., Vannier, M., et al. 2019, A&A, 627, A23

Farahi, A., Evrard, A. E., Rozo, E., Rykoff, E. S., & Wechsler, R. H. 2016, MNRAS, 460, 3900

Fazio, G. G., Hora, J. L., Allen, L. E., et al. 2004, ApJS, 154, 10

Fixsen, D. J. 2009, ApJ, 707, 916

Flaugher, B., Diehl, H. T., Honscheid, K., et al. 2015, AJ, 150, 150

Flender, S., Bleem, L., Finkel, H., et al. 2016, ApJ, 823, 98

Flewelling, H. A., Magnier, E. A., Chambers, K. C., et al. 2016, arXiv:1612.05243

Foreman-Mackey, D., Hogg, D. W., Lang, D., & Goodman, J. 2013, PASP, 125, 306

Gaia Collaboration, Brown, A. G. A., Vallenari, A., et al. 2018, A&A, 616, 1

Garg, A., Stubbs, C. W., Challis, P., et al. 2007, AJ, 133, 403

Geach, J. E., & Peacock, J. A. 2017, NatAs, 1, 795

George, E. M., Ade, P., Aird, K. A., et al. 2012, Proc. SPIE, 8452, 84521

George, E. M., Reichardt, C. L., Aird, K. A., et al. 2015, ApJ, 799, 177

Gioia, I. M., Maccacaro, T., Schild, R. E., et al. 1990, ApJS, 72, 567

Gonzalez, A. H., Gettings, D. P., Brodwin, M., et al. 2019, ApJS, 240, 33

Gralla, M. B., Crichton, D., Marriage, T. A., et al. 2014, MNRAS, 445, 460

Gralla, M. B., Gladders, M. D., Yee, H. K. C., & Barrientos, L. F. 2011, ApJ, 734, 103

Gralla, M. B., Marriage, T. A., Addison, G., et al. 2019, arXiv:1905.04592

Gruen, D., Seitz, S., Brimioulle, F., et al. 2014, MNRAS, 442, 1507

Gupta, N., Saro, A., Mohr, J. J., et al. 2017, MNRAS, 467, 3737

Habib, S., Heitmann, K., Higdon, D., Nakhleh, C., & Williams, B. 2007, PhRvD, 76, 083503

Habib, S., Pope, A., Finkel, H., et al. 2016, NewA, 42, 49

Hamilton-Morris, V., Smith, G. P., Edge, A. C., et al. 2012, ApJL, 748, L23

Hasselfield, M., Hilton, M., Marriage, T. A., et al. 2013, JCAP, 7, 8

Heitmann, K., Bingham, D., Lawrence, E., et al. 2016, ApJ, 820, 108

Heitmann, K., Finkel, H., Pope, A., et al. 2019, ApJS, 245, 16

Heitmann, K., Higdon, D., Nakhleh, C., & Habib, S. 2006, ApJL, 646, L1

Henderson, S. W., Allison, R., Austermann, J., et al. 2016, JLTP, 184, 772

Henning, J. W., Sayre, J. T., Reichardt, C. L., et al. 2018, ApJ, 852, 97

High, F. W., Stubbs, C. W., Rest, A., Stalder, B., & Challis, P. 2009, AJ, 138, 110

Hilton, M., Hasselfield, M., Sifón, C., et al. 2018, ApJS, 235, 20

Hoekstra, H., Herbonnet, R., Muzzin, A., et al. 2015, MNRAS, 449, 685

Hollowood, D. L., Jeltema, T., Chen, X., et al. 2019, ApJS, 244, 22

Hou, Z., Aylor, K., Benson, B. A., et al. 2018, ApJ, 853, 3

Huang, N., Bleem, L. E., Stalder, B., et al. 2019, arXiv:1907.09621

Itoh, N., & Nozawa, S. 2004, A&A, 417, 827

Jacobs, C., Collett, T., Glazebrook, K., et al. 2019, ApJS, 243, 17

Jimeno, P., Diego, J. M., Broadhurst, T., De Martino, I., & Lazkoz, R. 2018, MNRAS, 478, 638

Johnson, A., Blake, C., Amon, A., et al. 2017, MNRAS, 465, 4118

Johnston, D. E., Sheldon, E. S., Wechsler, R. H., et al. 2007, arXiv:0709.1159

Joudaki, S., Blake, C., Johnson, A., et al. 2018, MNRAS, 474, 4894

Keisler, R., Reichardt, C. L., Aird, K. A., et al. 2011, ApJ, 743, 28

Kelly, B. C. 2007, ApJ, 665, 1489

Khullar, G., Bleem, L. E., Bayliss, M. B., et al. 2019, ApJ, 870, 7

Klein, M., Grandis, S., Mohr, J. J., et al. 2019, MNRAS, 488, 739

Kneib, J.-P., & Natarajan, P. 2011, A&ARv, 19, 47

Koester, B. P., McKay, T. A., Annis, J., et al. 2007, ApJ, 660, 221

Kravtsov, A. V., & Borgani, S. 2012, ARA&A, 50, 353

Lin, Y., Partridge, B., Pober, J. C., et al. 2009, ApJ, 694, 992

Lin, Y.-T., & Mohr, J. J. 2004, ApJ, 617, 879

Liu, J., Hennig, C., Desai, S., et al. 2015a, MNRAS, 449, 3370

Liu, T., Tozzi, P., Tundo, E., et al. 2015b, ApJS, 216, 28

Lotz, J. M., Koekemoer, A., Coe, D., et al. 2017, ApJ, 837, 97

LSST Science Collaboration, Abell, P. A., Allison, J., et al. 2009, arXiv:0912.0201

Mainzer, A., Bauer, J., Cutri, R. M., et al. 2014, ApJ, 792, 30

Mann, A. W., & Ebeling, H. 2012, MNRAS, 420, 2120

Mantz, A., Allen, S. W., Rapetti, D., & Ebeling, H. 2010, MNRAS, 406, 1759

Mantz, A. B., Allen, S. W., Morris, R. G., et al. 2016, MNRAS, 463, 3582

Mantz, A. B., von der Linden, A., Allen, S. W., et al. 2015, MNRAS, 446, 2205

Maturi, M., Bellagamba, F., Radovich, M., et al. 2019, MNRAS, 485, 498

McClintock, T., Varga, T. N., Gruen, D., et al. 2019, MNRAS, 482, 1352

McDonald, M., Allen, S. W., Bayliss, M., et al. 2017, ApJ, 843, 28

Medezinski, E., Battaglia, N., Umetsu, K., et al. 2018, PASJ, 70, S28

Mehrtens, N., Romer, A. K., Hilton, M., et al. 2012, MNRAS, 423, 1024

Meisner, A. M., Lang, D., & Schlegel, D. J. 2017, AJ, 154, 161

Melin, J.-B., Bartlett, J. G., Cai, Z.-Y., et al. 2018, A&A, 617, A75

Melin, J.-B., Bartlett, J. G., & Delabrouille, J. 2006, A&A, 459, 341

Meneghetti, M., Bartelmann, M., Dahle, H., & Limousin, M. 2013, SSRv, 177, 31

Merloni, A., Predehl, P., Becker, W., et al. 2012, arXiv:1209.3114

Miknaitis, G., Pignata, G., Rest, A., et al. 2007, ApJ, 666, 674

Mocanu, L. M., Crawford, T. M., Vieira, J. D., et al. 2013, ApJ, 779, 61

Motl, P. M., Hallman, E. J., Burns, J. O., & Norman, M. L. 2005, ApJL, 623, L63

Murata, R., Nishimichi, T., Takada, M., et al. 2018, ApJ, 854, 120

Murata, R., Oguri, M., Nishimichi, T., et al. 2019, PASJ, 71, 107

Murphy, T., Sadler, E. M., Ekers, R. D., et al. 2010, MNRAS, 402, 2403

Muzzin, A., Wilson, G., Demarco, R., et al. 2013, ApJ, 767, 39

Navarro, J. F., Frenk, C. S., & White, S. D. M. 1996, ApJ, 462, 563

Newman, A. B., Belli, S., Ellis, R. S., & Patel, S. G. 2018, ApJ, 862, 125

Nozawa, S., Itoh, N., Kawana, Y., & Kohyama, Y. 2000, ApJ, 536, 31

Nurgaliev, D., McDonald, M., Benson, B. A., et al. 2013, ApJ, 779, 112

Nurgaliev, D., McDonald, M., Benson, B. A., et al. 2017, ApJ, 841, 5

Oguri, M., Lin, Y.-T., Lin, S.-C., et al. 2018, PASJ, 70, S20

Oke, J. B. 1974, ApJS, 27, 21

Persson, S. E., Murphy, D. C., Smee, S., et al. 2013, PASP, 125, 654

Petrillo, C. E., Tortora, C., Vernardos, G., et al. 2019, MNRAS, 484, 3879

Piffaretti, R., Arnaud, M., Pratt, G. W., Pointecouteau, E., & Melin, J.-B. 2011, A&A, 534, A109

Planck Collaboration, Adam, R., Ade, P. A. R., et al. 2015, A&A, 594, 1

Planck Collaboration, Adam, R., Ade, P. A. R., et al. 2016a, A&A, 594, A8

Planck Collaboration, Ade, P. A. R., Aghanim, N., et al. 2013, A&A, 550, A130
Planck Collaboration, Ade, P. A. R., Aghanim, N., et al. 2016b, A&A, 594, A27
Planck Collaboration, Ade, P. A. R., Aghanim, N., et al. 2016c, A&A, 594, A24
Planck Collaboration, Aghanim, N., Arnaud, M., et al. 2011, A&A, 536, A12
Planck Collaboration, Aghanim, N., Arnaud, M., et al. 2012, A&A, 543, A102
Planck Collaboration, Akrami, Y., Argüeso, F., et al. 2018, A&A, 619, A94
Predehl, P., Andritschke, R., Böhringer, H., et al. 2010, Proc. SPIE, 7732, 77320U
Raghunathan, S., Patil, S., Baxter, E., et al. 2019, ApJ, 872, 170
Rasmussen, C. E., & Williams, C. 2006, Gaussian Processes for Machine Learning (Cambridge, MA: MIT Press), http://www.gaussianprocess.org/gpml/
Reichardt, C. L., Stalder, B., Bleem, L. E., et al. 2013, ApJ, 763, 127
Repp, A., & Ebeling, H. 2018, MNRAS, 479, 844
Rest, A., Stubbs, C., Becker, A. C., et al. 2005, ApJ, 634, 1103
Rossetti, M., Gastaldello, F., Ferioli, G., et al. 2016, MNRAS, 457, 4515
Rozo, E., Bartlett, J. G., Evrard, A. E., & Rykoff, E. S. 2014, MNRAS, 438, 78
Rozo, E., & Rykoff, E. S. 2014, ApJ, 783, 80
Rozo, E., Rykoff, E. S., Bartlett, J. G., & Melin, J.-B. 2015, MNRAS, 450, 592
Rykoff, E. S., Rozo, E., Busha, M. T., et al. 2014, ApJ, 785, 104
Rykoff, E. S., Rozo, E., Hollowood, D., et al. 2016, ApJS, 224, 1
Sand, D. J., Treu, T., Ellis, R. S., & Smith, G. P. 2005, ApJ, 627, 32
Sanderson, A. J. R., Edge, A. C., & Smith, G. P. 2009, MNRAS, 398, 1698
Saro, A., Bocquet, S., Mohr, J., et al. 2017, MNRAS, 468, 3347
Saro, A., Bocquet, S., Rozo, E., et al. 2015, MNRAS, 454, 2305
Schaffer, K. K., Crawford, T. M., Aird, K. A., et al. 2011, ApJ, 743, 90
Schellenberger, G., & Reiprich, T. H. 2017, MNRAS, 469, 3738
Schlafly, E. F., Meisner, A. M., & Green, G. M. 2019, ApJS, 240, 30
Schlegel, D. J., Finkbeiner, D. P., & Davis, M. 1998, ApJ, 500, 525
Schwartz, D. A., Bradt, H. V., Remillard, R. A., & Tuohy, I. R. 1991, ApJ, 376, 424

Sehgal, N., Addison, G., Battaglia, N., et al. 2013, ApJ, 767, 38
Sharon, K., Bayliss, M. B., Dahle, H., et al. 2019, arXiv:1904.05940
Simet, M., McClintock, T., Mandelbaum, R., et al. 2017, MNRAS, 466, 3103
Simons Observatory Collaboration, Ade, P., Aguirre, J., et al. 2019, JCAP, 2019, 056
Skrutskie, M. F., Cutri, R. M., Stiening, R., et al. 2006, AJ, 131, 1163
Smail, I., Ellis, R. S., Fitchett, M. J., et al. 1991, MNRAS, 252, 19
Smith, G. P., Mazzotta, P., Okabe, N., et al. 2016, MNRAS, 456, L74
Soergel, B., Giannantonio, T., Efstathiou, G., Puchwein, E., & Sijacki, D. 2017, MNRAS, 468, 577
Song, J., Zenteno, A., Stalder, B., et al. 2012, ApJ, 761, 22
Spergel, D., Gehrels, N., Baltay, C., et al. 2015, arXiv:1503.03757
Stalder, B., Stark, A. A., Amato, S. M., et al. 2014, Proc. SPIE, 9147, 91473Y
Staniszewski, Z., Ade, P. A. R., Aird, K. A., et al. 2009, ApJ, 701, 32
Story, K., Aird, K. A., Andersson, K., et al. 2011, ApJL, 735, L36
Sunyaev, R., & Zel'dovich, Y. 1980, ARA&A, 18, 537
Sunyaev, R. A., & Zel'dovich, Y. B. 1972, CoASP, 4, 173
Tinker, J., Kravtsov, A. V., Klypin, A., et al. 2008, ApJ, 688, 709
Tody, D. 1993, in ASP Conf. Ser. 52, Astronomical Data Analysis Software and Systems II, ed. R. J. Hanisch, R. J. V. Brissenden, & J. Barnes (San Francisco, CA: ASP), 173
Vanderlinde, K., Crawford, T. M., de Haan, T., et al. 2010, ApJ, 722, 1180
Vikhlinin, A., Kravtsov, A. V., Burenin, R. A., et al. 2009, ApJ, 692, 1060
Voit, G. M. 2005, RvMP, 77, 207
von der Linden, A., Mantz, A., Allen, S. W., et al. 2014, MNRAS, 443, 1973
Weinberg, D. H., Mortonson, M. J., Eisenstein, D. J., et al. 2013, PhR, 530, 87
Wen, Z. L., Han, J. L., & Liu, F. S. 2012, ApJS, 199, 34
Wen, Z. L., Han, J. L., & Yang, F. 2018, MNRAS, 475, 343
Wright, E. L. 1979, ApJ, 232, 348
Wright, E. L., Eisenhardt, P. R. M., Mainzer, A. K., et al. 2010, AJ, 140, 1868
Zhang, Y., Jeltema, T., Hollowood, D. L., et al. 2019, MNRAS, 487, 2578
Zitrin, A., Broadhurst, T., Barkana, R., Rephaeli, Y., & Benítez, N. 2011, MNRAS, 410, 1939